ARL-TR-9019 ● AUG 2020

Aerodynamic Dataset Generation of a Long-Range Projectile

by Joseph D Vasile, Joshua T Bryson, Jubaraj Sahu, Justin L Paul, and Benjamin C Gruenwald

Approved for public release; distribution is unlimited.

NOTICES

Disclaimers

The findings in this report are not to be construed as an official Department of the Army position unless so designated by other authorized documents.

Citation of manufacturer's or trade names does not constitute an official endorsement or approval of the use thereof.

Destroy this report when it is no longer needed. Do not return it to the originator.

ARL-TR-9019 ● AUG 2020

Aerodynamic Dataset Generation of a Long-Range Projectile

Joseph D Vasile, Joshua T Bryson, Justin L Paul, and Benjamin C Gruenwald
Weapons and Materials Research Directorate, CCDC Army Research Laboratory

Jubaraj Sahu
Oak Ridge Associated Universities

Approved for public release; distribution is unlimited.

REPORT DOCUMENTATION PAGE

Form Approved
OMB No. 0704-0188

Public reporting burden for this collection of information is estimated to average 1 hour per response, including the time for reviewing instructions, searching existing data sources, gathering and maintaining the data needed, and completing and reviewing the collection information. Send comments regarding this burden estimate or any other aspect of this collection of information, including suggestions for reducing the burden, to Department of Defense, Washington Headquarters Services, Directorate for Information Operations and Reports (0704-0188), 1215 Jefferson Davis Highway, Suite 1204, Arlington, VA 22202-4302. Respondents should be aware that notwithstanding any other provision of law, no person shall be subject to any penalty for failing to comply with a collection of information if it does not display a currently valid OMB control number.
PLEASE DO NOT RETURN YOUR FORM TO THE ABOVE ADDRESS.

1. REPORT DATE *(DD-MM-YYYY)*	2. REPORT TYPE	3. DATES COVERED
August 2020	Technical Report	1 August 2019–1 April 2020

4. TITLE AND SUBTITLE
Aerodynamic Dataset Generation of a Long-Range Projectile

5a. CONTRACT NUMBER

5b. GRANT NUMBER

5c. PROGRAM ELEMENT NUMBER

6. AUTHOR(S)
Joseph D Vasile, Joshua T Bryson, Jubaraj Sahu, Justin L Paul, and Benjamin C Gruenwald

5d. PROJECT NUMBER

5e. TASK NUMBER

5f. WORK UNIT NUMBER

7. PERFORMING ORGANIZATION NAME(S) AND ADDRESS(ES)
CCDC Army Research Laboratory
ATTN: FCDD-RLW-LE
Aberdeen Proving Ground, MD 21005

8. PERFORMING ORGANIZATION REPORT NUMBER
ARL-TR-9019

9. SPONSORING/MONITORING AGENCY NAME(S) AND ADDRESS(ES)

10. SPONSOR/MONITOR'S ACRONYM(S)

11. SPONSOR/MONITOR'S REPORT NUMBER(S)

12. DISTRIBUTION/AVAILABILITY STATEMENT
Approved for public release; distribution is unlimited.

13. SUPPLEMENTARY NOTES
ORCID IDs: Joseph D Vasile, 0000-0003-3812-6277; Joshua T Bryson, 0000-0002-0753-6823; Jubaraj Sahu, 0000-0003-3347-4387; Benjamin C Gruenwald, 0000-0003-3968-5070; Justin Paul, 0000-0003-4133-7585

14. ABSTRACT
A comprehensive aerodynamic dataset of a tail-controlled projectile was generated to quickly evaluate and improve understanding of the flight performance of a long-range guided projectile. The method of compiling multiple aerodynamic data sources to generate the dataset of the vehicle was outlined. Navier–Stokes (CFD++) and inviscid (Cart3D) computational fluid dynamics results were combined with the semi-empirical aerodynamics prediction code (Missile DATCOM) in a formal manner to improve the accuracy of the aerodynamic model and coefficients. The database includes the effects of both aerodynamic pitch and roll as well as flap deflection on the flight vehicle across Mach number. The generated aerodynamic database underpins both 3- and 6-degrees-of-freedom flight-trajectory simulations.

15. SUBJECT TERMS
long-range guided projectiles, lift-to-drag, computational fluid dynamics, aerodynamic characterization, airframe design

16. SECURITY CLASSIFICATION OF:			17. LIMITATION OF ABSTRACT	18. NUMBER OF PAGES	19a. NAME OF RESPONSIBLE PERSON
					Joseph D Vasile
a. REPORT	b. ABSTRACT	c. THIS PAGE			19b. TELEPHONE NUMBER (Include area code)
Unclassified	Unclassified	Unclassified	UU	46	(410) 306-1794

Standard Form 298 (Rev. 8/98)
Prescribed by ANSI Std. Z39.18

Contents

List of Figures **v**

List of Tables **vi**

Acknowledgments **vii**

1. Introduction **1**

2. Vehicle Description **1**

2.1 Projectile Flight Body 1

2.1 Trailing-Edge Flap 2

3. Aerodynamic Sources **3**

3.1 Missile DATCOM 3

3.2 Cart3D 4

3.3 CFD++ 5

4. Technical Approach **7**

4.1 Full Airframe Characterization 7

4.2 Trailing-Edge Flap Deflection 8

4.3 Aerodynamic Roll Dependence 9

5. Database Generation **11**

5.1 Data Anchoring 11

5.2 Effect of Trailing-Edge Flap Deflection 17

5.3 Aerodynamic Dataset Methodology 19

5.3.1 Polynomial Regression of Aerodynamic Data 20

5.3.2 Spline Interpolation of Aerodynamic Data across Aerodynamic Roll Angle 23

6. Results and Discussion **23**

6.1 Comments and Future Work 28

6.2 Flow Visualization 29

7. Conclusion 32

8. References 33

List of Symbols, Abbreviations, and Acronyms 35

Distribution List 37

List of Figures

Fig. 1 Schematic of optimized projectile flight body for a 105-mm diameter, length-to-diameter of 10, and ogive length of 30% of overall length. Dimensions in millimeters. 2

Fig. 2 Numbering scheme and deflection sign convention for the trailing-edge control surfaces. View is from projectile base. 3

Fig. 3 Computational domain used for Cart3D 4

Fig. 4 Computational domain used for CFD++ 6

Fig. 5 Superimposed contour slices of streamwise velocity and surface pressure with the computational domain from Cart3D simulation for a single deflected trailing-edge flap, $\delta_3 = 20°$ for a given angle of attack, $\alpha = 8°$ 9

Fig. 6 Projectile flight body at aerodynamic roll angles, a) $\phi = 0°$, b) 22.5°, and c) 45°. View is from projectile base. 10

Fig. 7 a) Computed axial-force, b) normal-force and, and c) pitching-moment coefficients of the entire vehicle, computed by SEAP (solid lines), Cart3D (open triangle symbols), and CFD++ (open circle symbols) at $\phi = 0°$ 12

Fig. 8 a) Computed normal-force and b) pitching-moment coefficients of the entire vehicle, computed by SEAP (solid lines), Cart3D (open triangle symbols), and CFD++ (open circle symbols) at $\phi = 45°$ 13

Fig. 8 a) Computed normal-force and b) pitching-moment coefficients of the entire vehicle, computed by SEAP (solid lines), Cart3D (open triangle symbols), and CFD++ (open circle symbols) at $\phi = 45°$ 15

Fig. 9 Pitch-dampening-moment coefficient of projectile flight body without trailing-edge flap deflection computed by SEAP code (blue) and CFD++ (orange) at $\phi = 0°$, 22.5°, and 45°, and at $M_\infty = 2$ 16

Fig. 10 a) Roll-dampening-moment coefficient of projectile flight body and b) effect of single trailing-edge flap deflection on roll-dampening-moment coefficient 17

Fig. 11 Change in a) axial-force, b) normal-force, c) rolling-moment, and d) pitching-moment coefficients of the projectile flight body by trailing-edge flap deflection, δ_3, at $\phi = 0°$ and $M_\infty = 2$ 18

Fig. 12 Change in a) normal-force, b) side-force, c) pitching-moment, and d) yawing-moment coefficients of the projectile flight body by trailing-edge flap deflection, δ_3, at $\phi = 45°$ and $M_\infty = 2$ 19

Fig. 13 Example of polynomial regression (dashed lines) on FAS aerodynamic data (open circles) at $\phi = 0°$ and $M_\infty = 2$ 21

Fig. 14 Example of polynomial regression (dashed lines) on MAS aerodynamic data (open circles) at $\phi = 0°$ and $M_\infty = 2$ 22

Fig. 15 Computed static-aerodynamic coefficients of flight body projectile from generated aerodynamic dataset (solid lines) and CFD++ (dashed lines) across aerodynamic roll angle, at $\delta_i = 0$, $M_\infty = 2$, and $\alpha = 4°$.... 24

Fig. 16 Computed static aerodynamic coefficients of trailing-edge flap, δ_3, from generated aerodynamic dataset across aerodynamic roll angle at $\delta_i = 0$, $M_\infty = 2$, and $\alpha = 4°$ 25

Fig. 17 Computed static aerodynamic coefficients of flight body projectile from generated aerodynamic dataset (solid lines) and CFD++ (dashed lines) across aerodynamic roll angle at $\delta_i = 0$, $M_\infty = 2$, and $\alpha = 10°$... 26

Fig. 18 Computed static aerodynamic coefficients of trailing-edge flap, δ_3, from generated aerodynamic dataset across aerodynamic roll angle at $\delta_i = 0$, $M_\infty = 2$, and $\alpha = 10°$ 26

Fig. 19 Computed static aerodynamic coefficients of projectile flight body with trailing-edge flap deflection ($\delta_1 = 5°$ and $\delta_3 = -5°$) and corresponding flap component data of δ_3 at $\alpha = 0°$ (a and b) and $\alpha = 10°$ (c and d) at $M_\infty = 2$..... 27

Fig. 20 Computed static aerodynamic coefficients of projectile flight body with all trailing-edge flaps deflected ($\delta_i = 5°$) and corresponding flap component data of δ_3 at $\alpha = 0°$ (a and b) and $\alpha = 10°$ (c and d) at $M_\infty = 2$..... 28

Fig. 21 Surface contours of pressure coefficient superimposed with iso-surfaces of scaled Q-criterion ($Q_S = 1.5$) colored by streamwise vorticity at $\phi = 0°$ (a and b), $\phi = 22.5°$ (c and d), and $\phi = 45°$ (e and f) computed by Cart3D (a, c, and e) and CFD++ (b, d, and f) at $\alpha = 10°$ and $M_\infty = 2$ 30

List of Tables

Table 1 Summary of optimized design 2

Table 2 Roll-dampening-moment coefficient of projectile flight body computed by SEAP and CFD++ with trailing-edge flap deflection ... 16

Acknowledgments

The authors thank Dr Jim DeSpirito from the US Army Combat Capabilities Development Command (CCDC) Army Research Laboratory, for general discussions regarding flight dynamics and aerodynamic fundamentals, numerical techniques, and data processing routines. This work was supported in part by a grant of high-performance computing time from the US Department of Defense (DOD) High Performance Computing Modernization program at the CCDC Army Research Laboratory DOD Supercomputing Resource Center (DSRC), Aberdeen Proving Ground, Maryland, and the US Army Engineer Research and Development Center DSRC, Vicksburg, Mississippi.

1. Introduction

The process of aerodynamically characterizing a flight vehicle quickly as well as accurately is highly desirable for the rapid development of projectiles. Combining multiple aerodynamic data sources to produce an aerodynamic dataset is necessary to assess the flight behavior of long-range guided projectiles through flight trajectory simulations. Each aerodynamic source has its advantages and limitations; being able to combine them in a formal manner to characterize the flight vehicle requires subject matter expertise. The process of compiling aerodynamic sources with varying levels of fidelity to generate an aerodynamic dataset has previously been undertaken for a man-portable munition as well as an indirect gliding munition.[1,2] In the current effort, an improved analysis routine was developed to combine multiple computational aerodynamic data sources to quickly and accurately characterize the aerodynamics of a long-range projectile. Specifically, the semi-empirical aerodynamic prediction (SEAP) code Missile DATCOM,[3] NASA's Cartesian-mesh, Euler computational fluid dynamics (CFD) analysis package Cart3D,[4] and the Navier–Stokes CFD flow solver CFD++[5] were methodically used to quickly characterize the aerodynamics associated with long-range projectiles. The current analysis builds upon a preliminary aerodynamic dataset that was generated for a tail-controlled projectile in the "+", or plus orientation.[6–9] As the fidelity of the aerodynamic dataset improved, the aerodynamics of the vehicle proved to be highly roll-dependent. The goal of the current report is to provide insight into the methodology of compiling aerodynamic data sources of varying fidelity to adequately characterize long-range projectiles. The complete aerodynamic dataset includes static and dynamic aerodynamic coefficients that are pitch-, roll-, and trailing-edge-flap-dependent across Mach number.

2. Vehicle Description

2.1 Projectile Flight Body

An automated design optimization routine was developed and implemented to recommend aerodynamic characteristics (e.g., the size of the stabilizing and control surfaces) that maximized the lift-to-drag ratio for a given diameter, length-to-diameter ratio, and ogive length across the supersonic Mach number regime. More description on the optimization process can be found in Vasile et al.[6,7] The nose tip was modeled as a blunt nose defined by a bluntness radius that is 0.1 of the diameter (i.e., 0.1 cal.). The von Karman ogive nose shape was used, with the length of the ogive section defined to be 0.3 of the overall length (OAL) of the projectile. The

center of gravity of the flight vehicle was defined to be 0.6 of the OAL of the projectile. The body section was modeled as a constant axisymmetric cylinder. Additionally, a 7° boattail was modeled beginning 0.5 cal. forward of the base. The projectile was designed to be sabot launched from an 8-inch-diameter gun with no deploying aerodynamic surfaces. This requirement constrained the optimization to limit the fin span to 8 inches tip to tip. A leading-edge sweep angle of 83° was used. All control surfaces had a root thickness of 4 mm and tapered down to 2 mm at the tip. The optimized fin set design for a given body baseline configuration with a 105-mm diameter, 10-cal. length, and ogive length of 30% of the overall length of the projectile is summarized in Table 1 and illustrated in Fig. 1.

Table 1 Summary of optimized design

Vehicle configuration	Diameter (mm)	Length to diameter	Ogive length of OAL	No. of fins	Root fin chord (cal.)	Tip fin chord (cal.)	Fin span (cal.)
Body fin	105	10	0.3	4	6	2.2	1.935

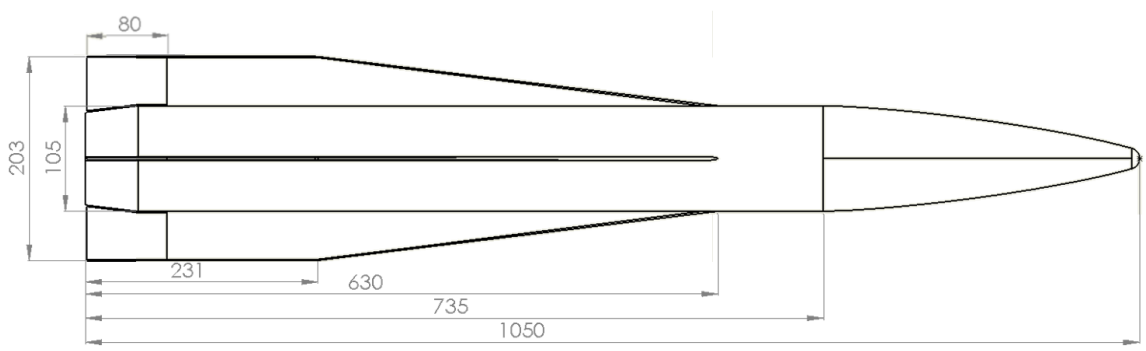

Fig. 1 Schematic of optimized projectile flight body for a 105-mm diameter, length-to-diameter of 10, and ogive length of 30% of overall length. Dimensions in millimeters.

Both static and dynamic aerodynamic coefficients were captured across Mach number, total angle of attack, aerodynamic roll angle, and trailing-edge flap deflection. These data were obtained from multiple aerodynamic data sources and techniques and are discussed further in the following sections.

2.1 Trailing-Edge Flap

To provide control during flight, trailing-edge flaps on each of the four fins rotated about the leading edge were employed. The control surface flaps are each 8 cm long and hinged at the flap leading edge. The size of the trailing-edge flaps was determined through a comprehensive control-surface design analysis that optimized flight performance (i.e., trim analysis) while meeting actuator requirements (i.e.,

hinge moments). More description of the control-surface analysis and development can be found in Bryson et al.[8,9] The numbering scheme of the control flaps as well as the deflection sign convention is presented Fig. 2. The sign convention of the trailing-edge control surfaces are such that when all trailing-edge flaps are deflected, a negative (i.e., counterclockwise) roll moment is produced.

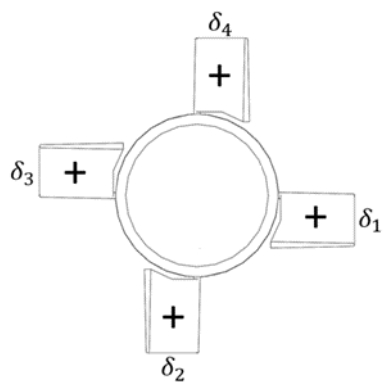

Fig. 2 Numbering scheme and deflection sign convention for the trailing-edge control surfaces. View is from projectile base.

3. Aerodynamic Sources

Multiple aerodynamic data sources from varying levels of fidelity were used to characterize the optimized projectile flight body. Moreover, each data source has an associated computational and human time cost. In general, lower-fidelity codes typically run on the order of minutes with minimal setup, whereas higher-fidelity codes require days of compute time with an equal amount of setup time. Ideally, the methodology employed will leverage and combine each data source to efficiently produce an aerodynamic dataset that accurately characterizes the flight body. The aerodynamic sources used, in increasing fidelity, were Missile DATCOM, Cart3D, and CFD++.

3.1 Missile DATCOM

Missile DATCOM (release 2014)[3] is an engineering-level computer program for estimating aerodynamic stability and control characteristics of conventional missile configurations. It uses both theoretical and empirical methods to encompass the entire speed regime from subsonic to hypersonic flight. The aerodynamic forces and moments at multiple flight conditions (i.e., M_∞, α, ϕ, and δ) for a given configuration can be typically computed in a matter of seconds. Due to its limited modeling capabilities, it is the least-accurate data source. However, at low angles of attack, where nonlinear effects are relatively negligible, Missile DATCOM produces a relatively accurate aerodynamic dataset foundation for a body-fin

configuration. Therefore, Missile DATCOM is leveraged to provide insight on trends of the aerodynamic coefficients for the undeflected trailing-edge flap configuration across flight conditions (i.e., M_∞, α, and ϕ).

3.2 Cart3D

NASA's Cart3D (1.5.5)[4] is an inviscid analysis package that allows for automated CFD analysis on complex aerodynamic designs. The Cartesian Euler CFD code was desirable because static aerodynamic coefficients for a given angle of attack could be computed in a matter of minutes. Cart3D quickly creates a Cartesian computational grid around the geometry after setting the domain's extent and resolution. The process uses adaptive mesh refinement (AMR) to increase fidelity of the meshed domain near small features and curvature of the geometry, thereby increasing the resolutions of the flow features present near the surface. The computational domain extended approximately 14 projectile lengths in all directions from the center of the projectile, and the smallest typical grid size for the domain was approximately 0.6 × 0.6 × 0.6 mm (Fig. 3). Mesh density regions were defined to refine the mesh near the surface as well as in the wake region to help resolve flow structures. These regions are further refined during the flow solution via the AMR. The computational domain consisted of approximately 10 million Cartesian cells. Once the mesh is generated, the flow solver (flowCart) exploits the features of the Cartesian grid to quickly compute the flow field and aerodynamic forces and moments experienced by the configuration. Since the Euler equations being solved do not include the viscous components, the Cart3D analysis package provides only inviscid aerodynamic coefficients.

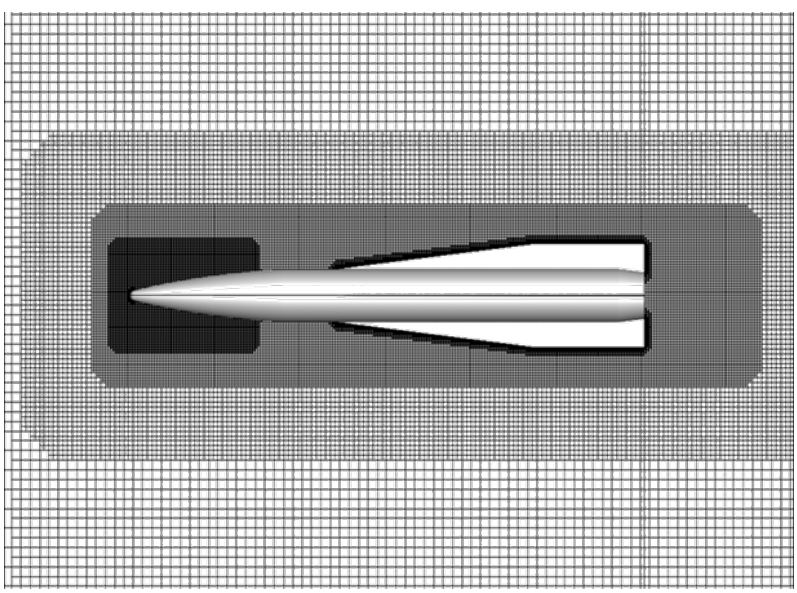

Fig. 3 Computational domain used for Cart3D

3.3 CFD++

The commercially available code, CFD++ v18.1.1 by Metacomp Technologies, Inc.[5] was used for all Navier–Stokes CFD simulations. The 3-D compressible Reynolds-averaged Navier–Stokes (RANS) equations were numerically solved to compute the flow solution. Steady-state and transient simulations were employed. The realizable k-ϵ two-equation turbulence model was used for all simulations. For the steady-state simulations, the solution was advanced toward convergence using a point-implicit time-integration scheme with local time-stepping, defined by the Courant–Friedrichs–Lewy (CFL) number. A linear ramping schedule was used to gradually increase the CFL number from 1 to 50 over the first 100 iterations, after which the CFL remained constant until convergence was reached. Implicit temporal smoothing was applied for the increased stability, which is especially useful where strong transients arise. The spatial discretization function was a second-order, upwind scheme using a Harten–Lax–van Leer–Contact Riemann solver and Metacomp's multidimensional total-variation-diminishing flux limiter.[10] Convergence for the total forces and moments was typically achieved in a few thousand iterations, with residuals reducing at six orders or more in magnitude. For the current study, initialization of the turbulence transport was completed by setting the turbulence intensity to 3% and the turbulent-to-molecular-viscosity ratio to 50, as the length scale was not known.

The computational domain used was generated using the Capstone (v9.1)[11] mesh generator. The total mesh size was approximately 43 M cells consisting of triangular surface cells with prism layers used along the surface and tetrahedral cells for the rest of the domain. The computational domain extended approximately 20 projectile lengths in all directions from the center of the projectile. The average cell size of the cylindrical density box (i.e., 2 cal. in radius, spanning 1 cal. forward to 5 cal. back of the projectile) was approximately 0.002 m. The first cell wall spacing of the prism layers was set to 3×10^{-7} m to ensure y^+ values of less than or equal to 1 along the surface of the projectile for all Mach numbers of interest. A close-up of the near-field of the computational domain used for CFD++ simulations is presented in Fig. 4.

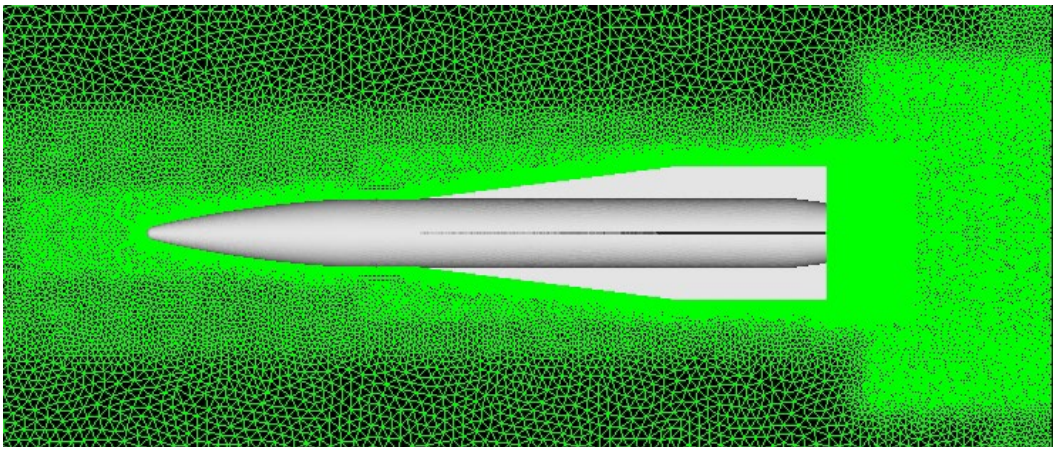

Fig. 4 Computational domain used for CFD++

Traditionally, aerodynamic information for projectiles has been obtained by computing the steady-state coefficients at multiple individual angles of attack. This method requires a lot of repetitive editing of input files, runs, and processing of computed results from these runs. In addition to steady-state simulations, a quasi-steady sweep procedure was employed that provides an easier method to consolidate the process and facilitates faster generation of aerodynamic data. More description on the quasi-steady sweep procedure can be found in Sahu and Fresconi.[12]

Time-accurate multidisciplinary coupled CFD/rigid body dynamics (RBD) computations were also employed to determine the dynamic aerodynamic coefficients. The coupled CFD/RBD procedure allows "virtual fly-out" of projectiles on the supercomputers as well as prediction of actual flight paths of a projectile and all the associated unsteady free-flight aerodynamics in an integrated manner. A time-accurate numerical approach is used in the coupled virtual fly-out simulations. This approach requires that the 6-degrees-of-freedom (6DOF) body dynamics be computed at each repetition of a flow solver. The CFD capability used here solves the same RANS equations and incorporates advanced boundary conditions and grid motion capabilities. For time-accurate simulations of virtual fly-outs, a dual time-stepping procedure is generally used to achieve the desired time accuracy in the time-accurate solutions. The whole grid was moved to take into account the motion of the projectile. To account for RBD, the grid point velocities were set as if the grid was attached to the rigid body with 6DOF. The dynamics are constrained by setting certain moments or forces to zero depending on the dynamics being isolated, hence the term "constraints-based". As an example, when examining the pitch-only motion at a specific Mach number, all forces and the roll and yaw moments are set to zero.

4. Technical Approach

4.1 Full Airframe Characterization

The full airframe was simulated and modeled using all of the previously described aerodynamic data sources. The SEAP aerodynamic data source was the most comprehensive dataset and therefore was used as the foundation of the generated aerodynamic dataset. The static and dynamic aerodynamic coefficients of the entire vehicle without trailing-edge flap deflection were modeled using the SEAP code across 17 Mach numbers (M_∞ = 0.1, 0.2, 0.4, 0.6, 0.8, 0.9, 1.02, 1.2, 1.5, 2, 3, 4, 5, 6, 7, 8, and 9), at 13 angles of attack (α = 0° to 20°, every 2°, α = 25°, and 30°), and at five aerodynamic roll angles (ϕ = 0° to 90°, every 22.5°).

To improve the overall fidelity of the dataset, the inviscid CFD analysis package Cart3D was used. A watertight solid model was created for the CFD solvers that was geometrically representative of the model used in the SEAP code. To account for the forces and moments of each trailing-edge flap, a 1.5-mm gap was used to separate the flaps to the rest of the body. The static forces and moments were found for the entire vehicle and each undeflected trailing-edge flap across 17 Mach numbers (i.e., M_∞ = 0.45, 0.55, 0.65, 0.75, 0.85, 0.95, 1, 1.02, 1.2, 1.5, 2, 2.5, 3, 3.5, 4, 6, 9), at 16 angles of attack (α = 0° to 20°, every 2°, and α = 25° to 45°, every 5°), and at five aerodynamic roll angles (ϕ = 0° to 90°, every 22.5°). All static forces moments computed from Cart3D, except axial force, were then applied to the aerodynamic dataset by updating the values of the original SEAP dataset. The updated coefficients were linearly interpolated across Mach and angle of attack at each aerodynamic roll angle. The axial force computed by the inviscid solver was not used since it is the least accurate, neglecting the contribution due to skin friction.

The Navier–Stokes CFD solver CFD++ was used to help anchor the aerodynamic dataset at a subset of flight conditions. Multiple steady-state simulations were performed that each spanned the different dimensions of the aerodynamic dataset to help improve the fidelity of the aerodynamic dataset. As described previously, a quasi-steady-state simulation sweep was performed to obtain the static forces and moments of the entire vehicle without trailing-edge flap deflection across 18 Mach numbers (M_∞ = 0.7, 0.8, 0.9, 0.92, 0.94, 0.96, 0.98, 1.05, 1.1, 1.2, 1.5, 2, 2.5, 3, 3.5, 4, 4.5, and 5), at four angles of attack (α = 0°, 2°, 5°, and 10°), and at two aerodynamic roll angles (ϕ = 0° and 45°). Since the Navier–Stokes simulations are highest in fidelity, all computed static forces and moments were applied to the Cart3D-updated aerodynamic dataset. As similarly performed for the Cart3D data, the aerodynamic data from CFD++ was linearly interpolated across Mach and angle

of attack at each aerodynamic roll angle. Since the CFD++ aerodynamic data did not extend to all flight conditions (e.g., high angle of attack), these data were not extrapolated. That is, the change in values between CFD++ and Cart3D/SEAP were clipped at the extents of the CFD++ dataset and applied to the rest of the dataset.

In addition to steady-state simulations, transient CFD simulations were performed to update the dynamic derivative values used in the aerodynamic dataset, specifically the pitch-dampening and roll-dampening moment coefficients. For pitch-dampening moment coefficient, a series of constrained pitch oscillating simulations of the entire vehicle without flap deflection was performed. The pitch oscillating simulations were performed at a single Mach number ($M_\infty = 2$) for three aerodynamic roll angles ($\phi = 0°$, 22.5°, and 45°). A nonlinear parameter estimation routine was applied to determine the pitch-dampening moment coefficient for each vehicle orientation. This routine requires evolution equations that contain an aerodynamic model. More description on the parameter estimation routine can be found in Sahu and Fresconi.[13] Similarly, for the roll-dampening-moment coefficient, a series of constrained rolling simulations of the entire vehicle with all four flap deflected was performed. The rolling simulations were performed at two Mach numbers ($M_\infty = 0.8$ and 2) for three flap-deflection angles ($\delta_{1-4} = 0°$, 4°, and 10°). The parameter estimation routine was used to determine the flap dependency on the roll-dampening-moment coefficient. The computed pitch-dampening-moment and roll-dampening-moment coefficients were then applied to the existing SEAP dampening-moment coefficients by adjusting the values across Mach and aerodynamic roll angle, respectively.

4.2 Trailing-Edge Flap Deflection

The aerodynamic data for the trailing-edge flap components were found using Cart3D by simulating a single trailing-edge flap (δ_3) in the plus orientation at multiple deflections ($\delta_3 = 0°$, 5°, 10°, 15°, 25°, and 30°) across all flight conditions. Although this technique has some limitations (e.g., capturing fin-on-fin interactions), by assuming independence and symmetry the number of CFD runs was significantly reduced to produce a reasonably accurate aerodynamic dataset. An example of the Cart3D simulation performed for the $\delta_3 = 20°$ trailing-edge flap is presented in Fig. 5. All static forces and moments were computed for each deflection angle and applied to the aerodynamic dataset. To capture the effect of flap deflection on the overall axial force of the vehicle, the increase in axial force for the single trailing-edge flap at each studied flap-deflection angle was computed. This change in the axial force was then superposed to the axial-force coefficient of the aerodynamic dataset. The trailing-edge flap data were then applied to the other

flaps and combined with the rest of the airframe as is discussed further in the following sections.

Based on the transient Navier–Stokes CFD simulations, it was found that the roll-dampening coefficient was also affected by trailing-edge flap deflection. As previously discussed, the airframe was modeled with all four flaps deflected (i.e., $\delta_{1-4} = 0°$, 4°, and 10°) for these constrained transient roll simulations. The computed roll-dampening coefficient was then applied to the dataset following the same process as described in the previous section.

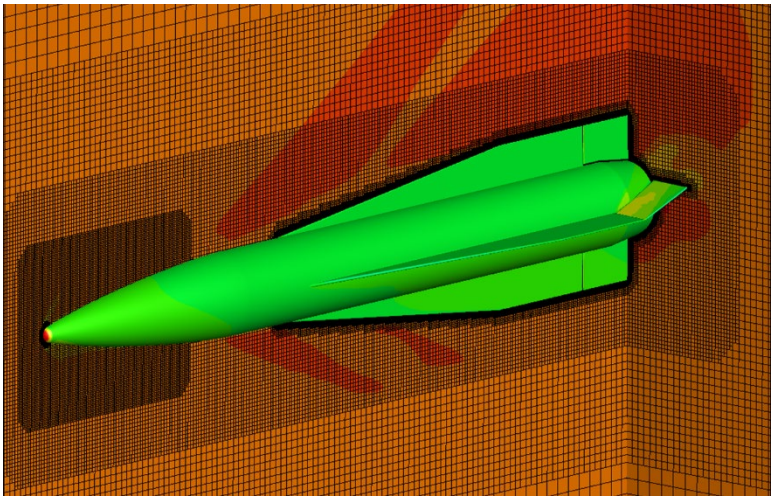

Fig. 5 Superimposed contour slices of streamwise velocity and surface pressure with the computational domain from Cart3D simulation for a single deflected trailing-edge flap, $\delta_3 = 20°$ for a given angle of attack, $\alpha = 8°$

4.3 Aerodynamic Roll Dependence

As the fidelity of the aerodynamic model improved with increased data analysis, the aerodynamic coefficients of the vehicle were shown to be highly roll-dependent. To accurately assess the vehicle's performance, a full aerodynamic roll characterization of the vehicle was performed. The static aerodynamic data for the entire airframe and all four trailing-edge flap components (no deflection; i.e., $\delta_i = 0°$) were obtained at multiple aerodynamic roll angles spanning from 0° to 90° every 22.5°. Since all four control flaps were tracked, symmetry was assumed such that all trailing-edge flaps could be mapped from 0° to 360°. Additionally, the pitch-damping and yaw-damping coefficients were captured by performing pitch-constrained oscillation simulations of the airframe without flap deflection at three aerodynamic roll angles, as presented in Fig. 6 (ϕ = 0°, 22.5°, and 45°). This methodology allowed for quick generation of an aerodynamic dataset that adequately captures aerodynamic roll dependency.

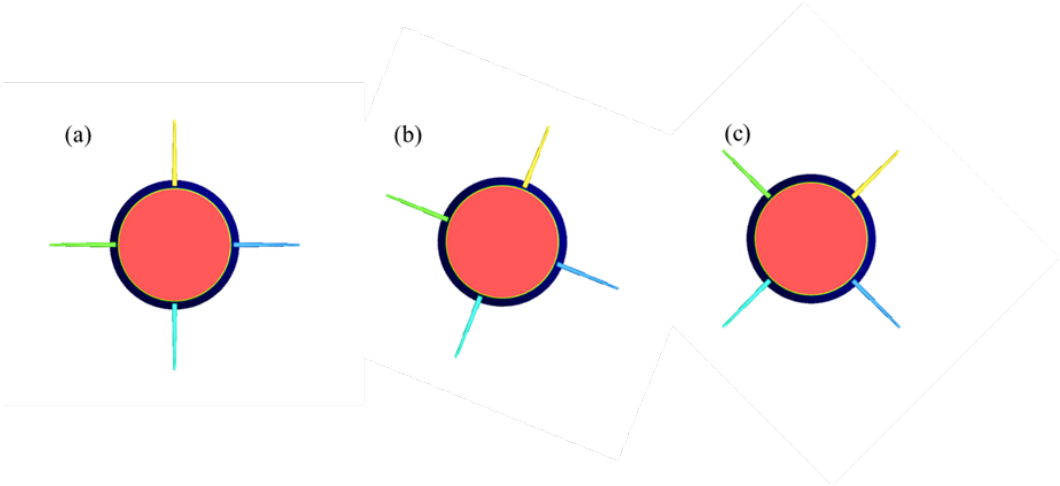

Fig. 6 Projectile flight body at aerodynamic roll angles, a) ϕ = 0°, b) 22.5°, and c) 45°. View is from projectile base.

To capture the roll dependency of flap deflection, the roll-dependent static aerodynamic data for the undeflected flap were adjusted using the flap-deflected static aerodynamic data computed in the "+" (i.e., plus) orientation. The process allows for an approximate accounting of the roll dependence on flap deflection without simulating the multiple flap deflection at multiple aerodynamic roll angles. The computed normal and side forces and moments from a deflected and undeflected flap were transformed and combined using superposition. The mapping of the forces and moments experienced by the undeflected flap across aerodynamic roll angle was used to interpolate the computed forces and moments contribution of flap deflection at ϕ = 0°. An example of capturing the forces and moments of a single trailing-edge flap (δ_3) deflected at an aerodynamic roll angle (ϕ = 0° to 90°) is presented in Eqs. 1–6.

$$C_{A_{\delta_3}}(\delta,\alpha) = C_{A_{\delta_3}}(0,\alpha) + \left(C_{A_{\delta_3}}(\delta,\alpha) - C_{A_{\delta_3}}(0,\alpha)\right) \tag{1}$$

$$C_{N_{\delta_3}}(\delta,\phi,\alpha) = C_{N_{\delta_3}}(0,\phi,\alpha) + \left(C_{N_{\delta_3}}(\delta,0,\alpha) - C_{N_{\delta_3}}(0,0,\alpha)\right)\cdot\cos\phi + \left(C_{S_{\delta_3}}(\delta,0,\alpha) - C_{S_{\delta_3}}(0,0,\alpha)\right)\cdot\sin\phi \tag{2}$$

$$C_{S_{\delta_3}}(\delta,\phi,\alpha) = C_{S_{\delta_3}}(0,\phi,\alpha) + \left(C_{S_{\delta_3}}(\delta,0,\alpha) - C_{S_{\delta_3}}(0,0,\alpha)\right)\cdot\cos\phi + \left(C_{N_{\delta_3}}(\delta,0,\alpha) - C_{N_{\delta_3}}(0,0,\alpha)\right)\cdot\sin\phi \tag{3}$$

$$C_{l_{\delta_3}}(\delta,\phi,\alpha) = C_{l_{\delta_3}}(0,\phi,\alpha) + \left(C_{l_{\delta_3}}(\delta,0,\alpha) - C_l(0,0,\alpha)\right) \tag{4}$$

$$C_{m_{\delta_3}}(\delta,\phi,\alpha) = C_{m_{\delta_3}}(0,\phi,\alpha) + \left(C_{m_{\delta_3}}(\delta,0,\alpha) - C_{m_{\delta_3}}(0,0,\alpha)\right)\cdot\cos\phi + \left(C_{n_{\delta_3}}(\delta,0,\alpha) - C_{n_{\delta_3}}(0,0,\alpha)\right)\cdot\sin\phi \tag{5}$$

$$C_{n_{\delta_3}}(\delta,\phi,\alpha) = C_{n_{\delta_3}}(0,\phi,\alpha) + \left(C_{n_{\delta_3}}(\delta,0,\alpha) - C_{n_{\delta_3}}(0,0,\alpha)\right)\cdot\cos\phi + \left(C_{m_{\delta_3}}(\delta,0,\alpha) - C_{m_{\delta_3}}(0,0,\alpha)\right)\cdot\sin\phi \tag{6}$$

The same process was performed for the rest of the flaps with each respective aerodynamic roll angle range: ϕ = 90° to 180° (δ_4), ϕ = 180° to 270° (δ_1), and ϕ = 270° to 360° (δ_2). As previously discussed, the process allowed for the complete mapping of each trailing-edge flap from ϕ = 0° to 360°.

5. Database Generation

5.1 Data Anchoring

As previously discussed, the data from each of the data sources were then methodically combined to create an aerodynamic dataset of coefficients. Since the Navier–Stokes CFD aerodynamic source was the highest in fidelity, the data computed were used to anchor the dataset. The static forces and moments for the entire vehicle, computed from all aerodynamic sources at multiple angles of attack across Mach number at two aerodynamic roll angles (i.e., ϕ = 0° and 45°), are presented in Figs. 7 and 8, respectively. The aerodynamic coefficients computed by SEAP are presented as solid lines, the coefficients computed by Cart3D presented as open triangle symbols, and the coefficients computed by CFD++ presented by open circle symbols. The aerodynamic dataset was then updated to match the values computed from Cart3D and CFD++ at each respective data point in that specific order. The adjustments were then linearly interpolated across the dataset. Any data outside of the Cart3D or CFD++ dataset were not extrapolated but rather were applied the same change in value from the last remaining data point in the higher-fidelity dataset. This allowed for the dataset to continue Mach number trends found from SEAP.

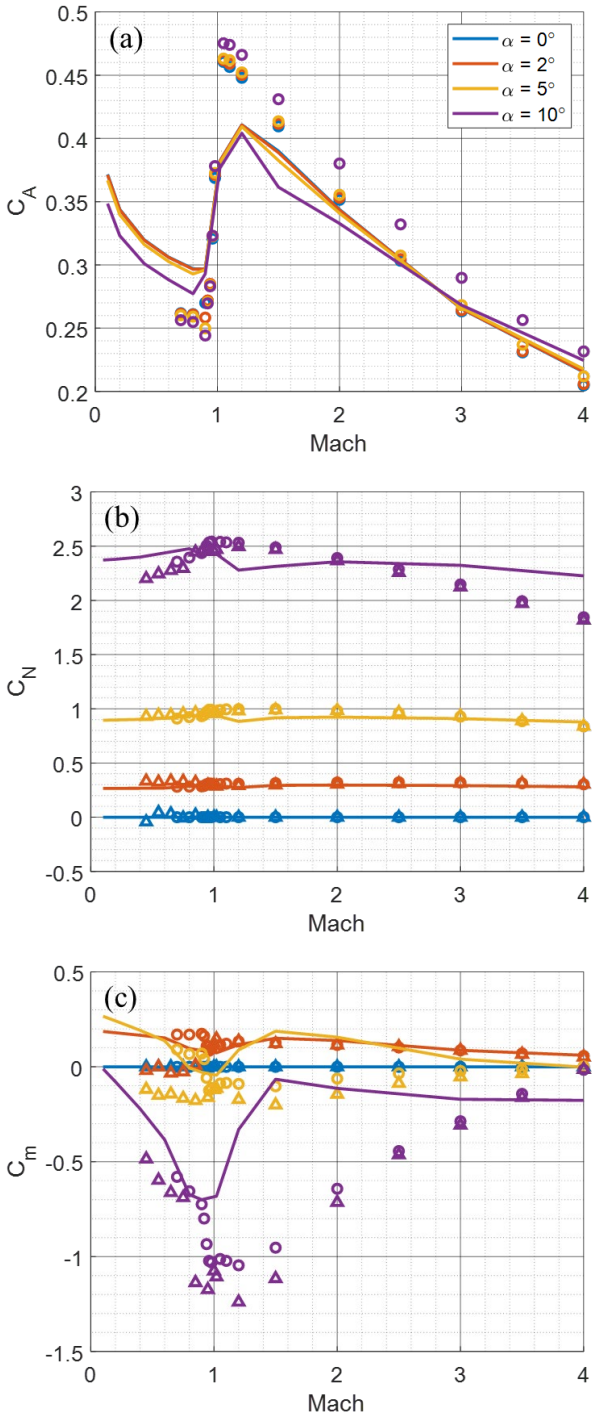

Fig. 7 a) Computed axial-force, b) normal-force and, and c) pitching-moment coefficients of the entire vehicle, computed by SEAP (solid lines), Cart3D (open triangle symbols), and CFD++ (open circle symbols) at $\phi = 0°$

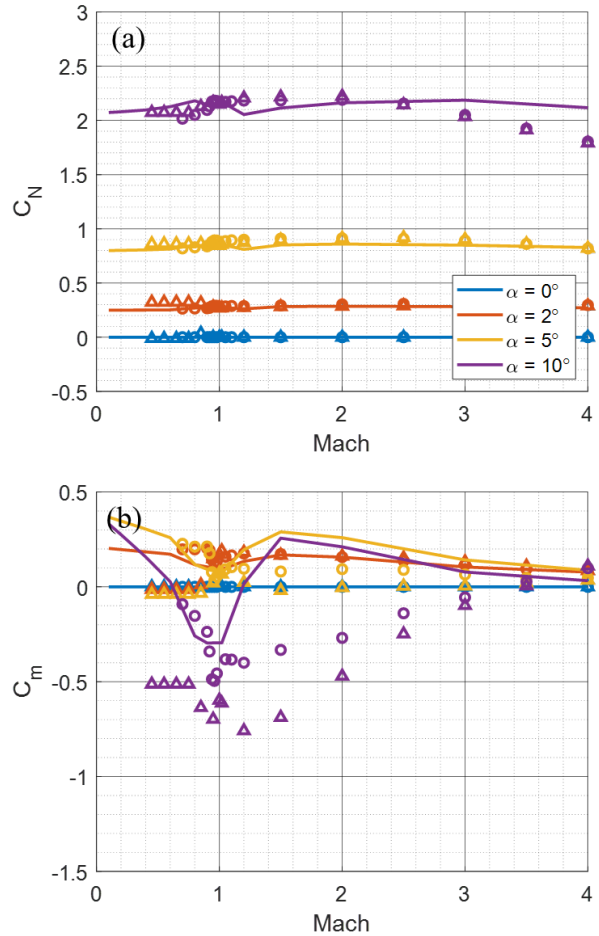

Fig. 8 a) Computed normal-force and b) pitching-moment coefficients of the entire vehicle, computed by SEAP (solid lines), Cart3D (open triangle symbols), and CFD++ (open circle symbols) at ϕ = 45°

The SEAP dataset overpredicts the axial force coefficient of the vehicle in the subsonic region compared with the CFD++ data (Fig. 7a). In the supersonic region the SEAP dataset generally underpredicts the axial-force coefficient up to Mach 2, then compares reasonably well at the lower angles of attack. However, the axial-force coefficient trend across Mach number compares relatively well. Since the Cart3D is an inviscid flow solver, the computed axial-force coefficient was not used. As stated previously, the SEAP axial-force coefficient was then adjusted and linearly interpolated across Mach number and angle of attack to match the values computed by CFD++.

Overall, all aerodynamic sources show reasonable agreement for normal-force coefficient (Fig. 7b), with more discrepancy at the higher angle of attack. The results suggest that SEAP code is suitable to accurately predict the normal-force coefficient for low-aspect-ratio finned projectiles at low and moderate angles of attack ($\alpha \leq 5°$). At higher angles of attack, the values deviate, suggesting that

high-angle-of-attack nonlinear flow physics are present and are not well-predicted in the SEAP code.

The largest discrepancies are observed for the predicted pitching-moment coefficients (Fig. 7c). The main contributor to this effect is the difference in the predicted location of the center of pressure between Missile DATCOM and the CFD codes. Although the normal force was accurately predicted, the center of pressure location and therefore pitching moment were not predicted well. Overall, the CFD results show larger values of pitching moment, specifically at higher angles of attack. Excellent agreement is observed at $\alpha = 2°$ in the supersonic range. The results suggest that SEAP may provide a more conservative (i.e., center of pressure location predicted further forward, therefore reduced stability) result when determining the static stability of low-aspect-ratio finned projectiles. Overall, at the current aerodynamic roll angle ($\phi = 0°$), Cart3D and CFD++ compare reasonably well. The largest discrepancies are present at subsonic and low supersonic speeds (Fig. 7c). At higher Mach numbers, the Reynolds number is very high, where viscous effects become less significant.

As previously discussed, the vehicle was found to have significant roll dependence as the fidelity of the dataset improved. The axial force is relatively unchanged by roll angle and therefore not plotted in Fig. 8. The normal-force and pitching-moment coefficient distributions of the entire vehicle at an aerodynamic roll angle of 45° are presented in Figs. 8a and 8b, respectively. As was shown previously, the normal force is predicted well by all aerodynamic sources. The SEAP prediction also shows improved prediction at $\alpha = 10°$. At $\phi = 45°$ the normal-force coefficient decreases approximately 10% compared with $\phi = 0°$. As discussed in Section 6.2, the addition of lifting surfaces exposed to the flow results in the generation of vortical structures that advect downstream near the body of the projectile. This exposed the projectile body to the flow changes, causing a change in pressure distribution as well as the center of pressure location of the entire vehicle. This is shown in the significant reduction in pitching-moment coefficient at the same flight conditions (Fig. 8b). The results show an approximate reduction of 40% in pitching-moment coefficient compared with the $\phi = 0°$ orientation. This finding is important for projectile designers, as the static pitching-moment coefficient is used to evaluate a vehicle's static stability. The design of the vehicle can dramatically change depending upon stability requirements, and therefore any proposed design for low-aspect-ratio finned projectiles require a full aerodynamic roll characterization.

The most noteworthy discovery is the large discrepancies of computed pitching-moment coefficient between the two CFD predictions (Fig. 8b). As was expected for the SEAP dataset, the SEAP code is unable to accurately predict the pitching-moment coefficient. The Cart3D results show a significant overprediction

(approximately 40%) of the pitching-moment coefficient magnitude compared with CFD++ at higher angles of attack across Mach number. The results suggest that viscous effects, specifically the viscous roll-up of vortical structures, play an important part in the computed pitching-moment coefficient. Further details and insights on the flow physics are presented in Section 6.2. Although Cart3D is routinely used for the rapid development of high-speed projectiles and has been generally performed well compared with higher-fidelity CFD results, further caution must be taken at certain flight conditions where near-body vortical structures and certain other viscous effects could be prevalent.

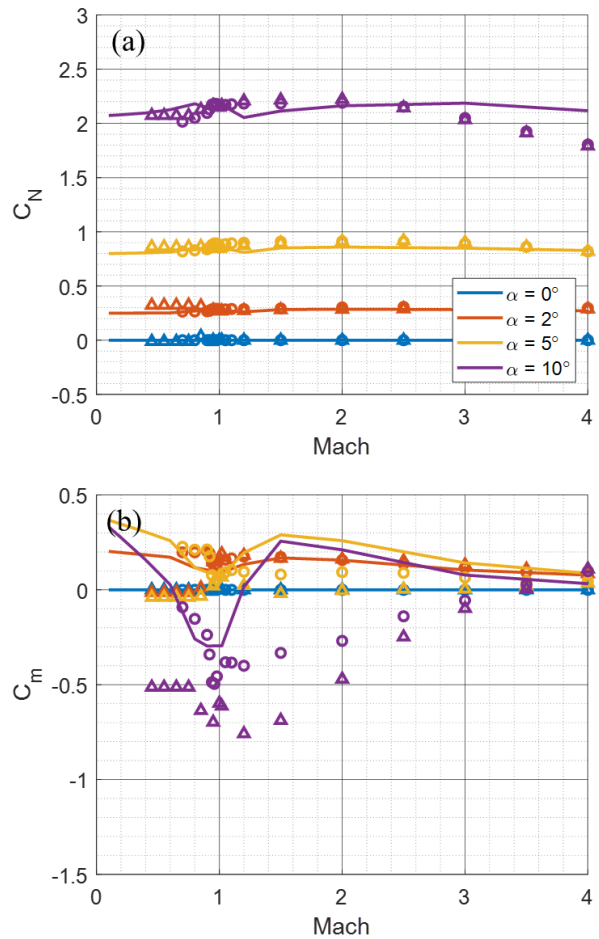

Fig. 9 a) Computed normal-force and b) pitching-moment coefficients of the entire vehicle, computed by SEAP (solid lines), Cart3D (open triangle symbols), and CFD++ (open circle symbols) at ϕ = 45°

In addition to static aerodynamic coefficients, dynamic aerodynamic coefficients were computed from time-accurate CFD simulations. These dynamic derivatives were then used to adjust and update the existing aerodynamic dataset across flight conditions. The pitch-dampening-moment coefficient was computed from constrained pitch oscillating simulations of the entire vehicle. The

pitch-dampening-moment coefficient computed from SEAP and CFD++ of the flight vehicle without flap deflection at three aerodynamic roll angles, $\phi = 0°$, 22.5°, and 45°, and at Mach 2 is presented in Fig. 9. Overall, the CFD++ data show the SEAP code underpredicts pitch-dampening-moment coefficient, and show that there is a roll dependence. The pitch-dampening-moment coefficient computed from CFD++ was then applied across the SEAP dataset in the same manner as previously discussed.

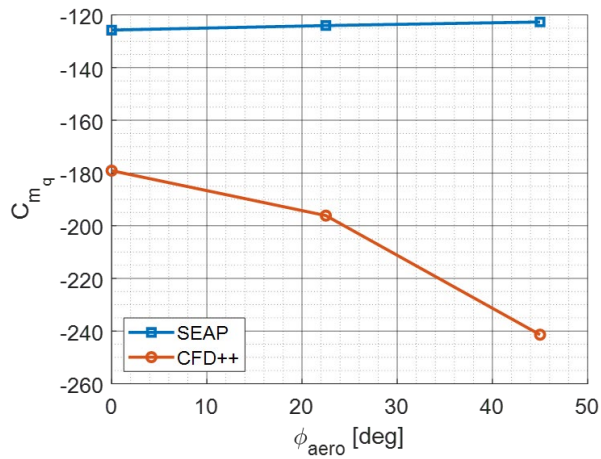

Fig. 10 Pitch-dampening-moment coefficient of projectile flight body without trailing-edge flap deflection computed by SEAP code (blue) and CFD++ (orange) at $\phi = 0°$, 22.5°, and 45°, and at $M_\infty = 2$

The roll-dampening-moment coefficient was computed by CFD++ through a time-accurate constrained roll motion simulation. All trailing-edge flaps were deflected and simulated at 0° angle of attack. The computed roll-dampening-moment coefficient at Mach 2 is presented in Table 2.

Table 2 Roll-dampening-moment coefficient of projectile flight body computed by SEAP and CFD++ with trailing-edge flap deflection

C_{l_p}	SEAP	CFD++
$\delta_{1\text{-}4} = 0°$	–7.178	–7.242
$\delta_{1\text{-}4} = 4°$	–7.178	–3.594
$\delta_{1\text{-}4} = 10°$	–7.178	–6.882

At zero trailing-edge flap deflection ($\delta_{1\text{-}4} = 0°$), the SEAP code compares favorably well to the higher-fidelity computed value. However, the SEAP code is unable to predict the roll-dampening-moment coefficient dependency on trailing-edge flap deflection. For small-to-moderate deflection angles, increasing flap deflection reduces the roll-dampening-moment coefficient magnitude. The CFD++ data was applied to the aerodynamic dataset in the same manner as previously discussed (i.e.,

transformed and interpolated across flight conditions). The roll-dampening-moment coefficient used the aerodynamic data is presented in Fig. 10a. Additionally, to isolate the effect of a single trailing-edge flap on the roll-dampening-moment coefficient, the change in roll-dampening moment was equally divided by 4. The effect of a single trailing-edge flap, δ_3, on the roll-dampening-moment coefficient for the projectile flight body is presented in Fig. 10b.

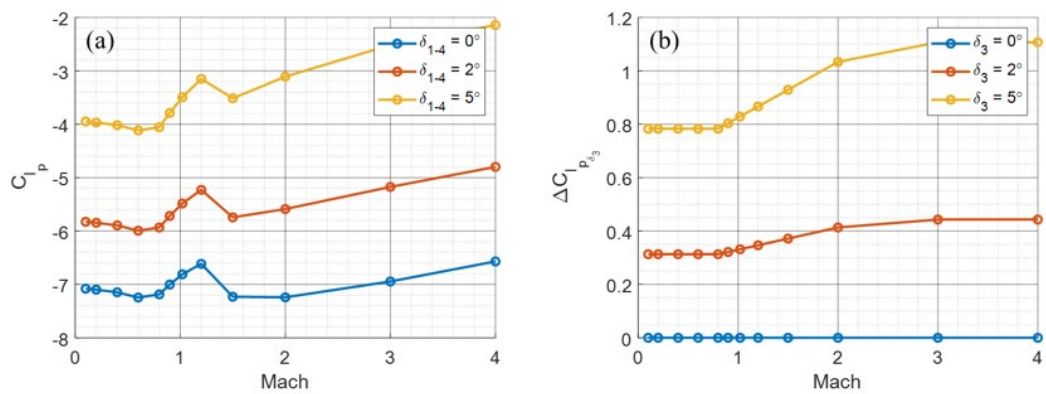

Fig. 11 a) Roll-dampening-moment coefficient of projectile flight body and b) effect of single trailing-edge flap deflection on roll-dampening-moment coefficient

5.2 Effect of Trailing-Edge Flap Deflection

As previously discussed, the trailing-edge flap components were found using Cart3D by simulating a single trailing-edge flap (δ_3) in the "+" (i.e., plus) orientation at multiple deflections across all flight conditions. To maintain the overall fidelity of the aerodynamic dataset, the effect of flap deflection was computed by subtracting the zero flap deflection component value from the deflected trailing-edge flap component value. By implementing this process, it was assumed that any errors associated with the inviscid solver would be reduced, specifically the computed axial-force coefficient. It was assumed that the additional axial-force contribution due to flap deflection is mainly driven by pressure drag; therefore, the axial-force change from undeflected to defected flap computed from Cart3D would provide a reasonable prediction of drag increase due to flap deflection. Presented in Fig. 11 is the change in noteworthy static force and moment coefficients for the entire flight body vehicle by a single trailing-edge flap at six flap deflections (δ_3 = 0° , 5°, 10°, 15°, 25°, and 30°) across angle of attack at $\phi = 0$ and Mach 2. The lateral-plane coefficients are zero for this configuration. As expected, with positive flap deflection all forces and moments increase in magnitude. The axial-force and pitching-moment coefficients of the entire vehicle increases and the normal-force and rolling-moment coefficients decrease (see Fig. 2). Furthermore, the results suggest that at low flap deflection angles, there is

less of an angle of attack dependence; however, nonlinear behaviors become more prevalent at higher angles of flap deflection.

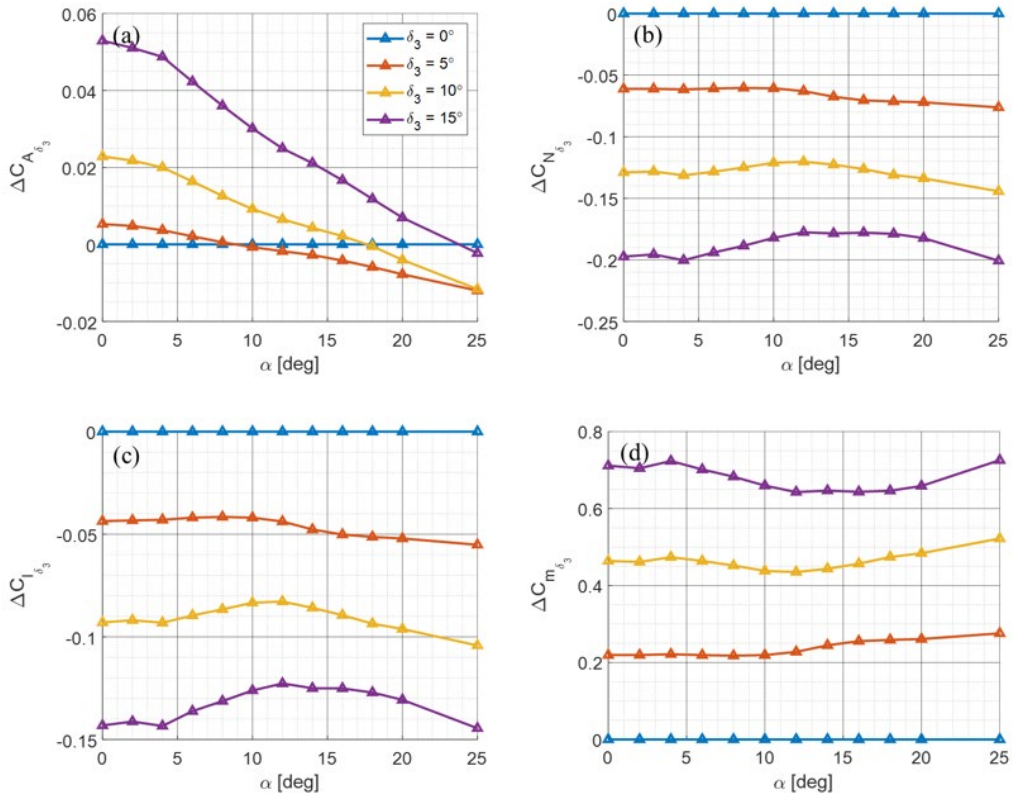

Fig. 12 Change in a) axial-force, b) normal-force, c) rolling-moment, and d) pitching-moment coefficients of the projectile flight body by trailing-edge flap deflection, δ_3, at $\phi = 0°$ and $M_\infty = 2$

Since the deflected trailing-edge flap component data was only collected in the plus orientation, the effect of aerodynamic roll angle on flap deflection was estimated by implementing the method outlined previously in Eqs. 1–6. The relationship of aerodynamic roll angle on the undeflected trailing flaps was used to adjust the deflected trailing-edge flap component data. The estimated effect of flap deflection for a single flap, δ_3, at $\phi = 45°$ and the same flight conditions described, is presented in Fig. 12. It was assumed that the axial-force and rolling-moment contributions due to flap deflection would be negligible across aerodynamic roll angle, and therefore were not altered. Overall, the magnitude of the longitudinal-plane aerodynamic coefficients are reduced at the prescribed aerodynamic roll angle, though it is recovered in the lateral-plane aerodynamic coefficients. The overall relationship of flap deflection across total angle of attack is preserved.

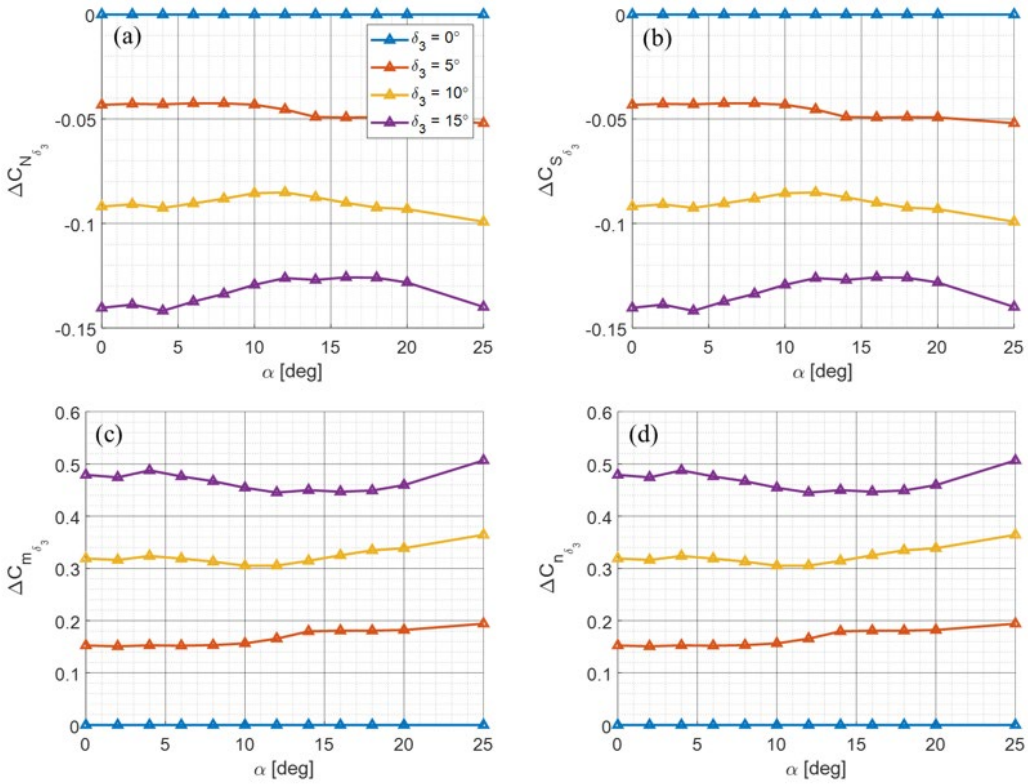

Fig. 13 Change in a) normal-force, b) side-force, c) pitching-moment, and d) yawing-moment coefficients of the projectile flight body by trailing-edge flap deflection, δ_3, at ϕ = 45° and M_∞ = 2

5.3 Aerodynamic Dataset Methodology

To simplify the implementation of the aerodynamic dataset into 6-DOF flight trajectory simulations, the aerodynamic data describing the forces and moments due to the movable trailing-edge flaps, termed movable aerodynamic surfaces (MASs), are applied separately from the aerodynamic data for the assembly of the body and fixed fin surfaces, referred to as fixed aerodynamic surfaces (FASs). Moreover, the MAS aerodynamic model is populated with coefficients that depend on the i^{th}control surface, δ_i, component. The FAS aerodynamic data were computed by subtracting the MAS aerodynamic data from the entire flight vehicle aerodynamic data. Through this methodology, the individual deflections of each trailing-edge flap across flight conditions can be combined to the FAS aerodynamic data to estimate the entire projectile flight body aerodynamics. The individual deflections of Flap 1 to Flap 4 are superimposed to determine the body angle of attack and lateral acceleration due to varying MAS deflections. For example, at ϕ = 0°, following the convention shown in Fig. 2 to produce a positive, upward pitch deflection, δ_q is defined in Eq. 7.

$$\delta_q = -\delta_1 + \delta_3 \tag{7}$$

5.3.1 Polynomial Regression of Aerodynamic Data

The aerodynamic data for each respective FAS and MAS was fitted using a polynomial fitting routine to regress the static forces and moment coefficients as a function of $\sin(\alpha)$ at each aerodynamic roll angle and Mach number. This allowed for easy reconstruction of the forces and moments of the flight body projectile at any given angle of attack. The normal-force and side-force, as well as pitching- and yawing-moment coefficients, were regressed with a 5th-order polynomial. The axial-force coefficient was regressed with a 4th-order polynomial, with only even terms used. The rolling-moment coefficient was fitted with a 2nd-order polynomial. An example of this process on the FAS and MAS aerodynamic data is presented in Figs. 13 and 14, respectively. The polynomial fit (dashed lines) is able to adequately capture the behavior of the dataset (open circles). The methodology allows for a more accurate computation of the static stability derivatives across angle of attack (e.g., C_{m_α}), which can be useful for flight stability analysis and flight control development.

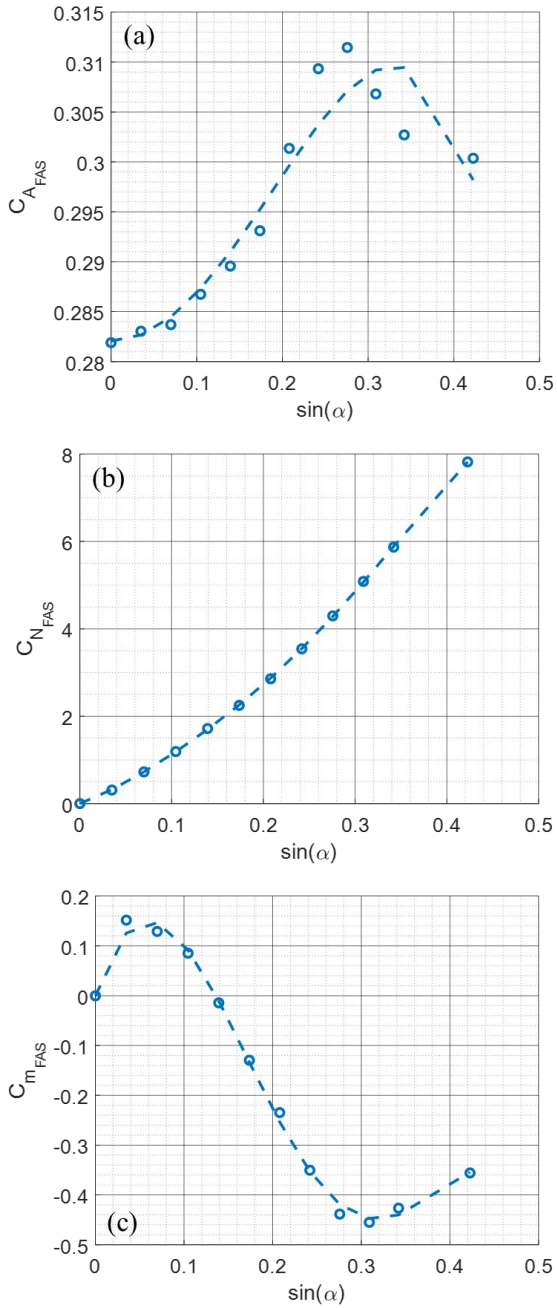

Fig. 14 Example of polynomial regression (dashed lines) on FAS aerodynamic data (open circles) at $\phi = 0°$ and $M_\infty = 2$

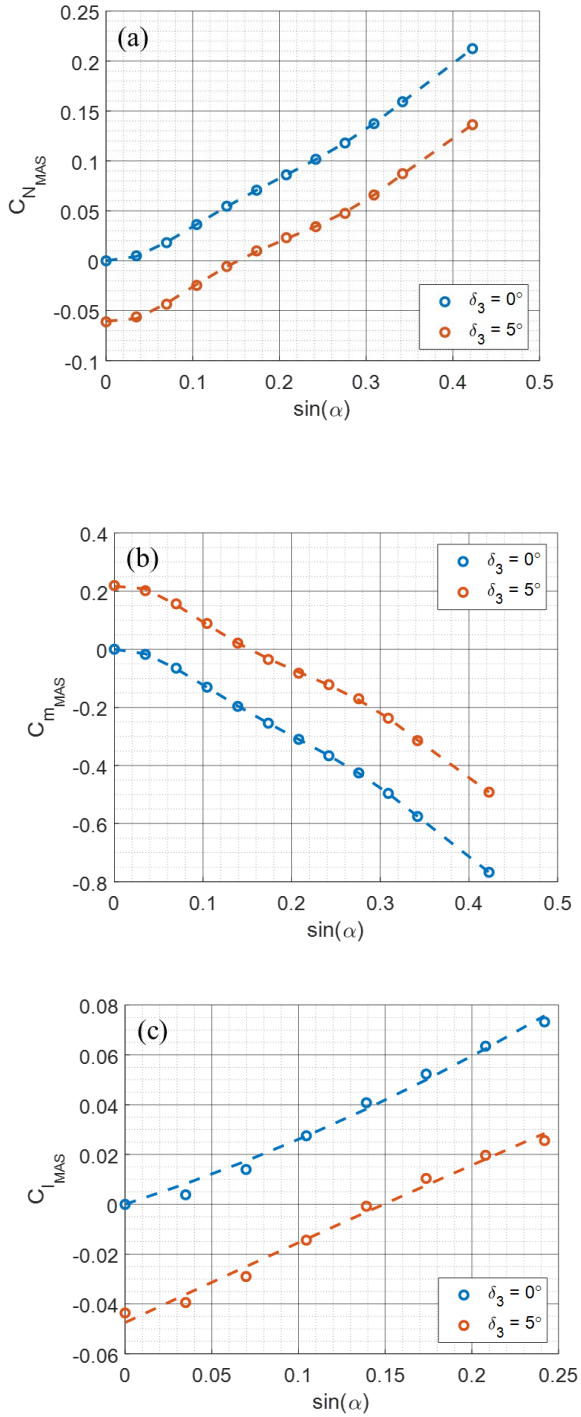

Fig. 15 Example of polynomial regression (dashed lines) on MAS aerodynamic data (open circles) at $\phi = 0°$ and $M_\infty = 2$

5.3.2 Spline Interpolation of Aerodynamic Data across Aerodynamic Roll Angle

The methodology of compiling, reshaping, and polynomial regressing the aerodynamic data was performed at 17 aerodynamic roll angles (ϕ = 0° to 360°, every 22.5°). A spline interpolation routine was implemented across aerodynamic roll angle to improve the resolution of the aerodynamic data for use in 6-DOF flight trajectory simulation. A spline interpolator was used to preserve the shape and behavior of the data across aerodynamic roll angle. The spline interpolation improved the resolution of the data to a total of 129 aerodynamic roll angles, or every 2.8125°.

6. Results and Discussion

An aerodynamic dataset was generated by methodically combining data from multiple computational aerodynamic sources to characterize a long-range projectile flight body across all flight conditions (i.e., M_∞, α, ϕ, and δ). The complete aerodynamic coefficient dataset was produced through a combination of superposition and linear and spline interpolation. An example of the generated dataset of the flight body projectile with zero trailing-edge flap deflection at $M_\infty = 2$ and $\alpha = 4°$ versus aerodynamic roll angle is presented Fig. 15. An independent steady-state simulation study was performed using CFD++ to compare and verify that the roll dependency of the generated aerodynamic dataset was captured correctly. A series of steady-state simulations was performed at 17 aerodynamic roll angles (ϕ = 0° to 90°, every 5.625°) and is presented alongside to the generated aerodynamic dataset in Fig. 15 (dashed lines). Note all coefficients in the following figures are in the nonrolled flight dynamics body frame.

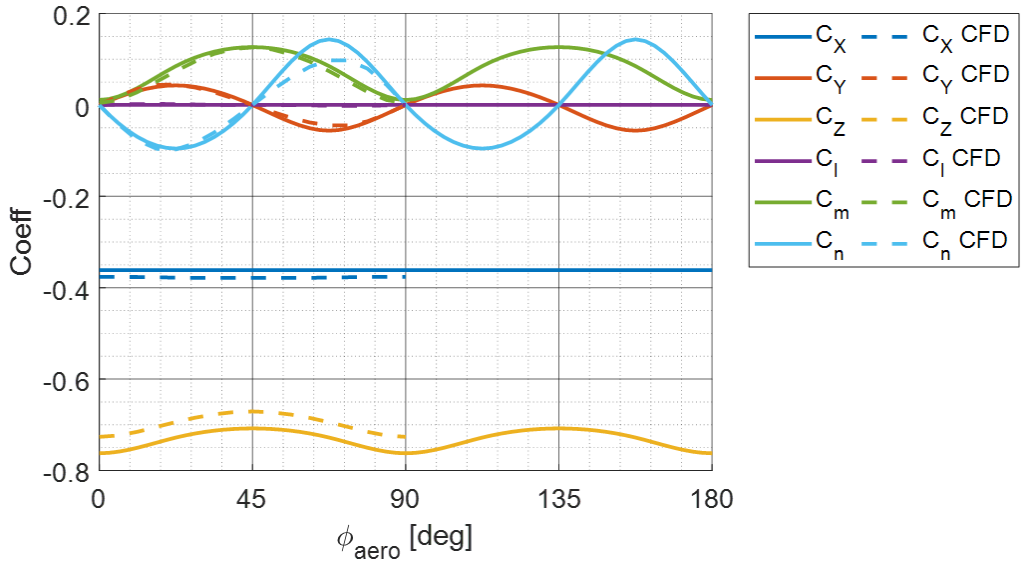

Fig. 16 Computed static-aerodynamic coefficients of flight body projectile from generated aerodynamic dataset (solid lines) and CFD++ (dashed lines) across aerodynamic roll angle, at $\delta_i = 0$, $M_\infty = 2$, and $\alpha = 4°$

As was indicated in Figs. 7 and 8, Fig. 15 shows that the projectile flight body is aerodynamic-roll-dependent. The aerodynamic roll distribution follows trigonometric functions; the longitudinal forces and moments are out of phase with respect to the lateral forces and moments. The out-of-plane forces and moments are at a maximum when the geometry of the projectile flight body is asymmetric to the incoming flow. The fins of the projectile generate asymmetric vortical structures, which induce a side force and corresponding moment. More details of the flow physics are presented in Section 6.2.

Overall, the generated aerodynamic dataset compares well with the CFD++ results. The behavior of the aerodynamic roll angle distribution was adequately captured. The results show that projectile flight body aerodynamic forces and moments are symmetric across aerodynamic roll angle, therefore the assumption of symmetry during the dataset generation seems to be reasonable. Moreover, since the distribution as well as magnitudes are relatively similar, the method of superposing FAS and MAS aerodynamic data as well as polynomial regression with each interpolation routine appears to be a valid process in characterizing the projectile flight body.

The aerodynamic coefficients computed by the generated dataset for a single trailing-edge flap at zero flap deflection ($\delta_3 = 0°$) across aerodynamic roll angle at $M_\infty = 2$ and $\alpha = 4°$ is presented in Fig. 16. Due to the nature of the methodology implemented to compute the trailing-edge flap components, the static aerodynamic coefficients presented in Fig. 16 also include the effect of the upstream FAS on the

MAS (i.e., the trailing-edge flap component with the presence of the body). The results show the trailing-edge flap coefficients are highly roll-dependent and symmetry cannot be assumed. The most-noteworthy finding is the effect angle of attack has, specifically windward versus leeward, on the trailing-edge flap components. The results show that the trailing-edge flap is both aerodynamic-roll-angle- and angle-of-attack-dependent. Using Fig. 16, the total MAS contribution at a given aerodynamic roll angle can be easily computed. For example, the total MAS contribution of all trailing-edge flaps at $\phi = 0°$ can be quickly computed by adding the coefficient value of δ_3 at $\phi = 180°$, $\phi = 270°$, $\phi = 0°$, and $\phi = 90°$, which correspond to δ_1, δ_2, δ_3, and δ_4 at $\phi = 0°$, respectively.

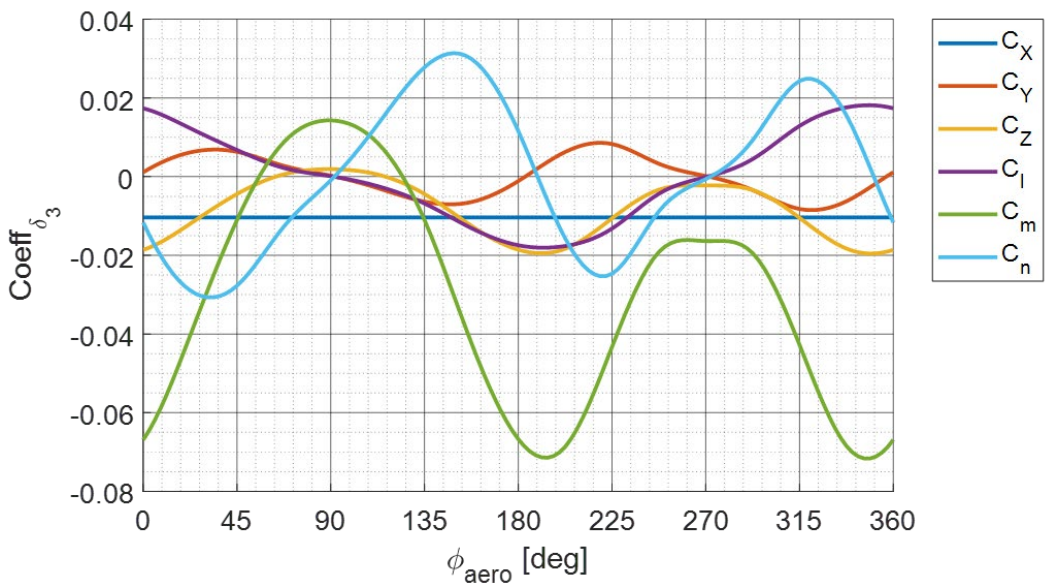

Fig. 1 Computed static aerodynamic coefficients of trailing-edge flap, δ_3, from generated aerodynamic dataset across aerodynamic roll angle at $\delta_i = 0$, $M_\infty = 2$, and $\alpha = 4°$

Presented in Figs. 17 and 18, respectively, are the computed aerodynamic coefficient of the flight body projectile with zero trailing-edge flap deflection and corresponding flap component δ_3 across aerodynamic roll angle at $M_\infty = 2$ at $\alpha = 10°$. As performed at $\alpha = 4°$, an independent steady-state simulation study was also performed for the projectile flight body at $\alpha = 10°$. As expected, increasing angle of attack increases the magnitude of the aerodynamic coefficients. At this angle of attack, the generated aerodynamic dataset still compares favorably to the results from CFD++.

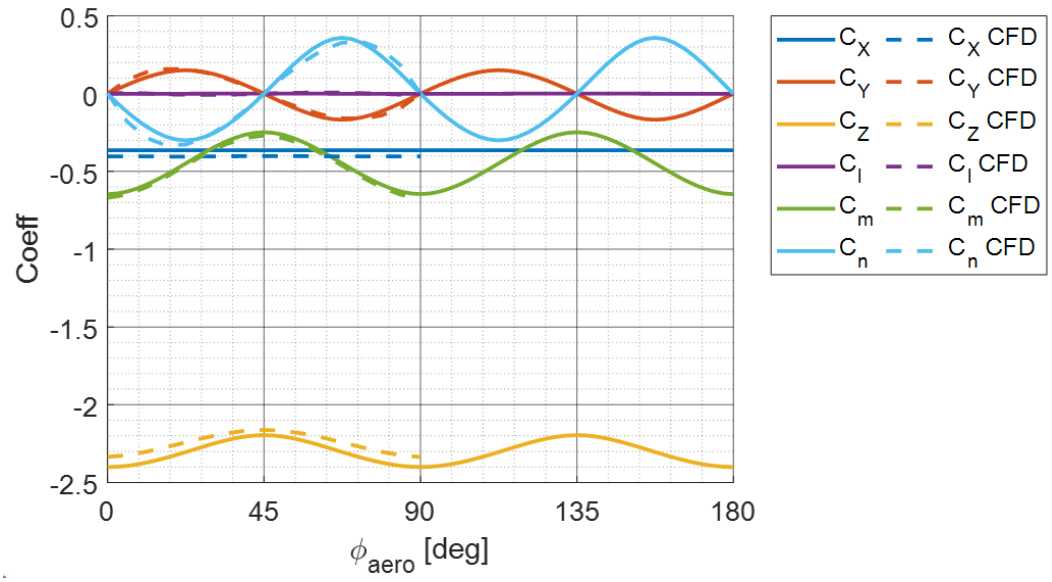

Fig. 17 Computed static aerodynamic coefficients of flight body projectile from generated aerodynamic dataset (solid lines) and CFD++ (dashed lines) across aerodynamic roll angle at $\delta_i = 0$, $M_\infty = 2$, and $\alpha = 10°$

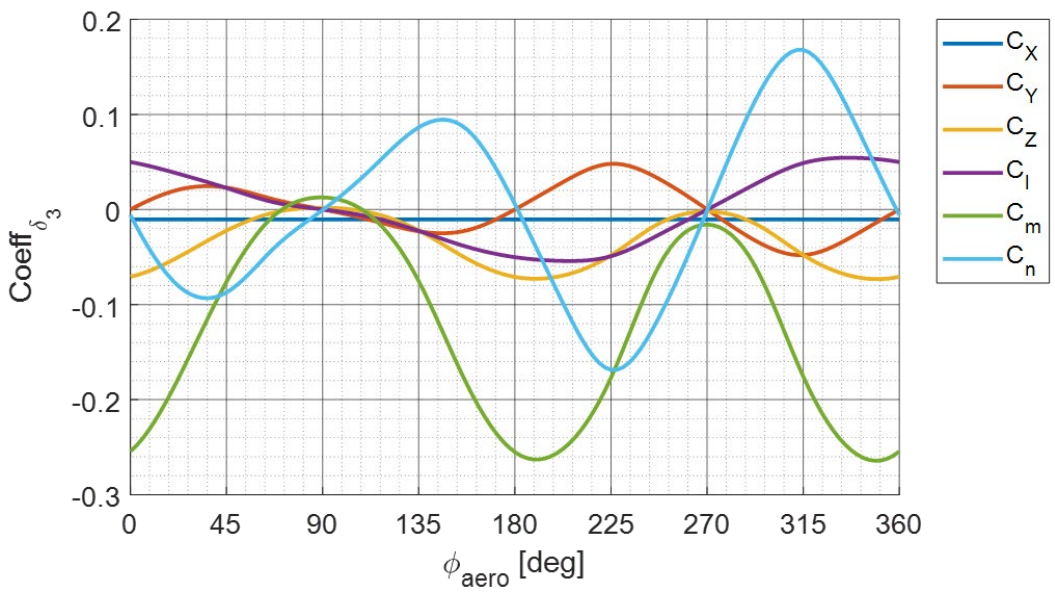

Fig. 18 Computed static aerodynamic coefficients of trailing-edge flap, δ_3, from generated aerodynamic dataset across aerodynamic roll angle at $\delta_i = 0$, $M_\infty = 2$, and $\alpha = 10°$

The effect of trailing-flap deflection on the projectile flight body across aerodynamic roll angle is presented in Figs. 19 and 20. Fig. 19 presents the effect of deflecting trailing-edge Flaps 1 and 3 (i.e., $\delta_1 = 5°$ and $\delta_3 = -5°$) as described in Eq. 7 at $\alpha = 0°$ (Fig. 19a and b) and $\alpha = 10°$ (Fig. 19c and d) at $M_\infty = 2$. At $\alpha = 0°$, non-negligible aerodynamic coefficients of the projectile flight body are generated by the superposition of δ_1 and δ_3. Since both flaps are deflected equally and in the

same direction, the total roll moment of the vehicle is zero. At ϕ = 0°, 180°, and 360°, the trailing-edge flaps produce an in-plane force in the vertical direction, causing a pitching moment. At ϕ = 90° and 270°, the trailing-edge flaps cause an out-of-plane force in the horizontal direction, causing a yawing moment. At α = 0°, it can be easily observed that the distribution of the aerodynamic coefficients follow trigonometric function behavior (Fig. 19a). At α = 10°, an asymmetry behavior from ϕ = 0° to ϕ = 180° is observed (Fig. 19c). As similarly observed for the undeflected flap, the aerodynamic coefficient components of the deflected trailing-edge flap are highly roll-dependent at an angle of attack (Fig. 19d). The local incident angle of the trailing-edge flaps with the respect to the incoming flow changes depend upon aerodynamic roll angle, causing asymmetric forces and moments with respect to aerodynamic roll angle.

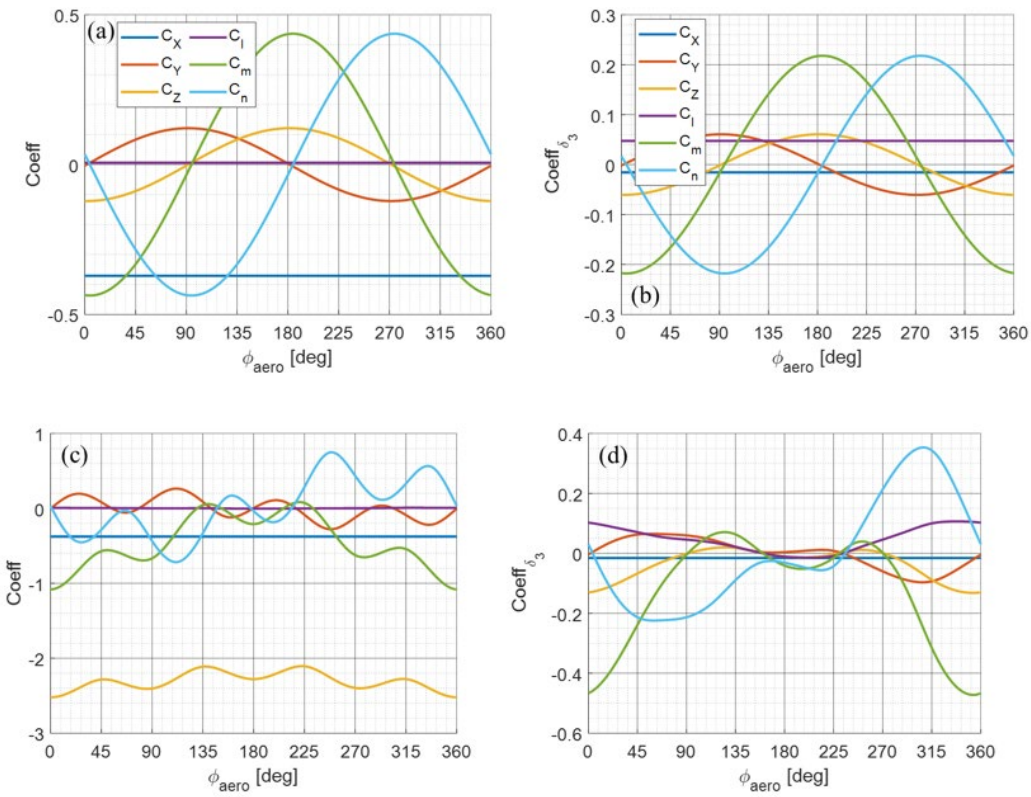

Fig. 19 Computed static aerodynamic coefficients of projectile flight body with trailing-edge flap deflection (δ_1 = 5° and δ_3 = -5°) and corresponding flap component data of δ_3 at α = 0° (a and b) and α = 10° (c and d) at M_∞ = 2

Figure 20 presents the effect of deflecting all trailing-edge flaps for roll (i.e., $\delta_1 = \delta_2 = \delta_3 = \delta_4 = -5°$) as described in Eq. 7 at α = 0° (Fig. 20a and b) and α = 10° (Fig. 20c and d) at M_∞ = 2. The aerodynamic coefficients of the trailing-edge flap are the same as Fig. 19 since δ_3 is deflected at the same angle and at the same flight conditions. The flap deflections produce a positive rolling moment (Fig. 20a).

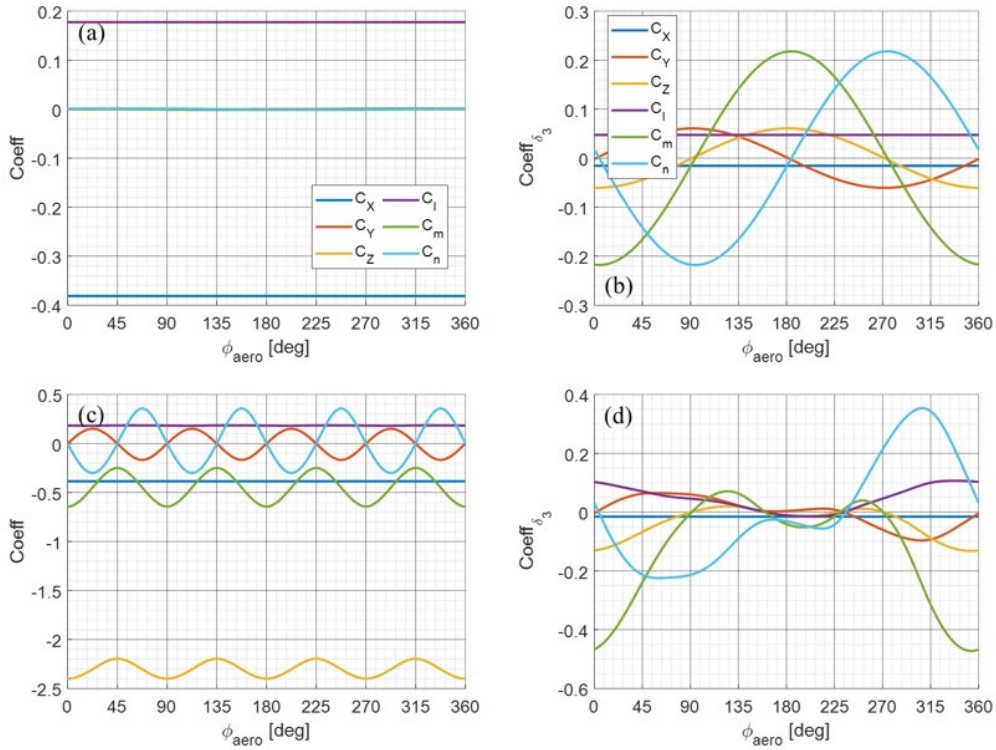

Fig. 20 Computed static aerodynamic coefficients of projectile flight body with all trailing-edge flaps deflected (δ_i = 5°) and corresponding flap component data of δ_3 at α = 0° (a and b) and α = 10° (c and d) at M_∞ = 2

6.1 Comments and Future Work

The results show that the methodology of superposing the aerodynamic data into FAS and MAS components, as well performing polynomial regression, provides the ability to quickly generate the aerodynamic data for the projectile flight body at different trailing-edge flap deflection configurations. However, since the MAS data is built upon a single trailing-edge flap, there may be inaccuracies in the dataset. It was assumed that the effect of multiple flaps deflected do not cause a cross-coupling effect (i.e., flap-on-flap interactions). Moreover, the deflected flap data were only captured at ϕ = 0°; the aerodynamic roll angle dependency of flap deflection was mapped by the undeflected trailing-edge flap data. An example scenario that is not currently captured is the effect on pitching moment from a trailing-edge flap deflected at ϕ = 90° at an appreciable angle of attack, α. The leeward trailing-edge flap may induce a significant pitching moment. This phenomena could be captured by either simulating flap deflection at multiple aerodynamic roll angles or simulating flap deflection at ϕ = 0° at multiple sideslip angles.

Future work planned includes additional CFD (i.e., inviscid and Navier–Stokes) to address the deficiencies of the dataset as described previously, as well as both spark

range and wind tunnel experimentation. The aerodynamic coefficients of the entire flight body projectile as well as the effect of trailing-edge flap deflection on the flight vehicle can be quantified across flight conditions. Through the use of both numerical and experimental data, the fidelity of the aerodynamic dataset will be further improved.

6.2 Flow Visualization

As was found through the full aerodynamic roll characterization of the projectile flight body, the aerodynamic coefficients at an appreciable angle of attack showed aerodynamic-roll-angle dependency. Furthermore, it was found that the static normal-force and pitching-moment coefficients reduced in magnitude and reached a minimum at $\phi = 45°$. At certain flight conditions, the reduced pitching-moment coefficient value caused the flight vehicle to become statically unstable. This behavior of swept low-aspect-ratio finned projectiles could prove problematic for designers when a projectile remains stable in one orientation (e.g., $\phi = 0°$) while becoming unstable in another orientation (e.g., $\phi = 45°$). Moreover, this issue can be exacerbated when implementing lower-fidelity aerodynamic data sources to quickly compute the aerodynamic coefficients. As was shown in Fig. 8, at $\phi = 45°$ the results from Cart3D overpredicted the static pitching-moment coefficient compared with the higher-fidelity results from CFD++. Conversely, at $\phi = 0°$ the pitching-moment coefficient computed from each aerodynamic data source compared favorably. The results suggest that there is a viscous flow phenomena that becomes significant when the lifting surfaces of the projectile are windward and leeward on the projectile with respect to the flow. To improve our understanding of the flow physics associated with long-range projectiles, the generation and advection of the vortical structures produced by the fins were studied.

Presented in Fig. 21 are qualitative plots of scaled Q-criterion iso-surfaces superimposed with contours of pressure coefficient on the surface of the flight body projectile with zero trailing-edge flap deflection, at $\alpha = 10°$ and $M_\infty = 2$, computed from Cart3D (Fig. 21a, c, and e) and CFD++ (Fig. 21b, d, and f), at $\phi = 0°$ (Fig. 21a and b), 22.5° (Fig. 21c and d) and 45° (Fig. 21e and f). The Q-criterion was developed to help isolate the vortex features from the vorticity present in the boundary layer by defining vortices in flows as spatial regions where the vorticity tensor dominates the rate of strain.[14] The scaled Q-criterion, Q_S, is mathematically expressed in Eq. 8.

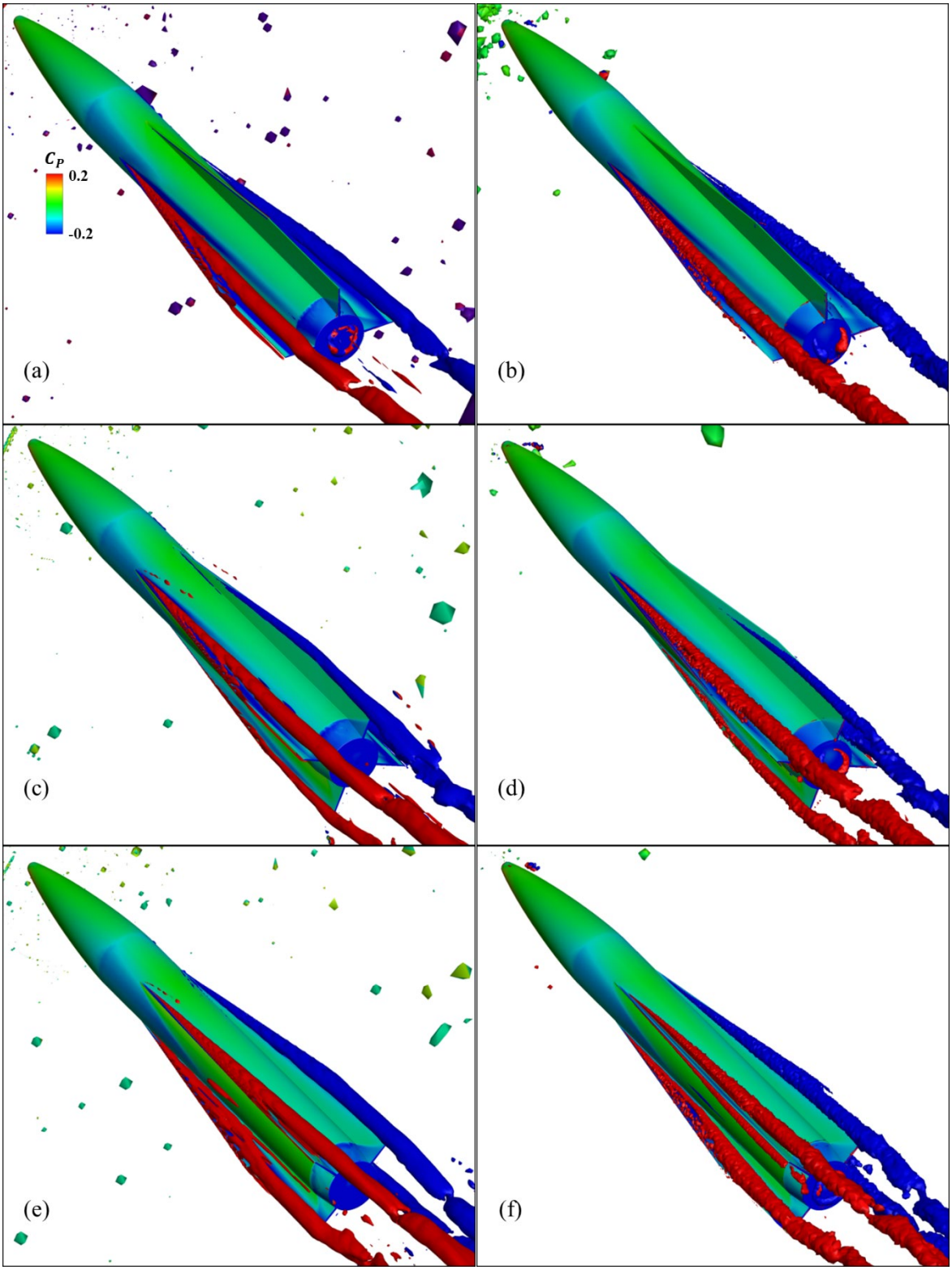

Fig. 21 Surface contours of pressure coefficient superimposed with iso-surfaces of scaled Q-criterion (Q_S = 1.5) colored by streamwise vorticity at ϕ = 0° (a and b), ϕ = 22.5° (c and d), and ϕ = 45° (e and f) computed by Cart3D (a, c, and e) and CFD++ (b, d, and f) at α = 10° and M_∞ = 2

$$Q_S = \frac{1}{2}\left(\frac{\|\boldsymbol{\Omega}\|^2}{\|\boldsymbol{S}\|^2} - 1\right), \tag{8}$$

where $\boldsymbol{\Omega}$ and $\boldsymbol{S}$ are the vorticity tensor and rate of strain tensor, respectively. The scaled Q-criterion iso-surfaces allow for visual observation of the vortical structures formed at the tip of the fins. The iso-surface value was set to 1.5. The iso-surface was colored based on the magnitude of streamwise vorticity at the same location. The surface pressure coefficient contour levels were set to be continuous between –0.2 and 0.2.

For all aerodynamic roll angles, vortical flow structures are generated along the leading edge of the swept portion the fin (Fig. 21). At $\phi = 0°$, two large vortical structures are generated along the fins that are perpendicular to the incoming flow. These flow structures advect downstream, increasing in size and magnitude. The vortical structures remain close to the fin and body, causing a reduction in pressure on the surfaces near the flow structure. This reduction of pressure increases the pressure difference across the fin, therefore increasing the lift of the vehicle. Rotating the projectile flight body to $\phi = 22.5°$ causes the generation of additional vortical structures on the additional fins exposed to the flow. However, due to the orientation of the fins, vortical structures are asymmetric in size and strength, therefore explaining the generation of a side force and yawing moment as observed in Fig.17. At $\phi = 45°$, all four fins are generating vortical flow structures symmetric in size and magnitude. Due to the presence of additional flow structures, the surface pressure distribution changes, therefore explaining the change in static force and moment coefficient.

The computed vortical flow structures predicted by Cart3D and CFD++ show good agreement. However, there are some discrepancies as the aerodynamic roll angle increases. This is natural since the inviscid code does not include the viscous roll-up as the vortex is formed along the fin tip. At $\phi = 45°$, the advection of the leeward vortical flow structures seem to deviate between the flow solvers, which could indicate there are differences in how the vortices are being generated. These small details could cause the surface pressure distribution to slight differ and therefore cause a small change in the predicted center of pressure location. However, that small difference can make a big difference in computed static-pitching-moment coefficient.

Further details on the flow physics associated with this airframe (including additional detailed flow visualizations), as well as an in-depth analysis of the roll-orientation-dependent aerodynamics can be found in Vasile and Sahu.[15]

7. Conclusion

A comprehensive effort was undertaken to produce a dataset of aerodynamic coefficients that are dependent on Mach, angle of attack, aerodynamic roll angle, and trailing-edge flap deflection for a low-aspect-ratio finned projectile. Multiple aerodynamic data sources of varying fidelity were used to analyze the projectile flight body. The aerodynamic data sources were compiled in a formal manner to improve the accuracy of the aerodynamic dataset used in flight trajectory simulations. The results showed that the flight vehicle was highly dependent on angle of attack, aerodynamic roll, and flap deflection. Moreover, it was observed that viscous effects became more prevalent for certain aerodynamic roll angles at high angle of attack. Overall, the generated aerodynamic dataset was able to adequately characterize the aerodynamics of the long-range projectile. Spark range and wind tunnel experiments are planned to address the limitations of the dataset as well as improve the overall aerodynamic model.

8. References

1. Vasile J, Fresconi F, Celmins I, Nelson B. Aerodynamic design optimization of control mechanisms for a subsonic, small diameter munition. Proceedings of the AIAA/ASCE/AHS/ASC Structures, Structural Dynamics, and Materials Conference; 2018 Jan 8–12; Kissimmee, FL. AIAA Paper No.: 2018-1654.

2. Bryson J, Vasile J, Celmins I, Fresconi F. Approach for understanding range extension of gliding indirect fire munitions. Aberdeen Proving Ground (MD): CCDC Army Research Laboratory (US); 2019 Aug. Report No.: ARL-TR-8753.

3. Rosema C, Doyle J, Blake W. Missile DATCOM user's manual, 2014 revision., Wright Patterson Air Force Base (OH): Flight Dynamics Directorate, Air Force Research Laboratory (US); 2014 Dec. Report No.: AFRL-RQ-WP-TR-2014-0281.

4. Aftosmis MJ, Berger MJ, Adomavicius G. A parallel multilevel method for adaptively refined Cartesian grids with embedded boundaries. Proceedings of the 38th AIAA Aerospace Sciences Meeting and Exhibit; 2000; Reno, NV. AIAA Paper No.: 2000-0808.

5. Metacomp Technologies, Inc. CFD++ user manual. Agoura Hills (CA): Metacomp; 2017.

6. Vasile J, Bryson J, Fresconi F. Aerodynamic design optimization of long range projectiles using Missile DATCOM. Proceedings of the AIAA Scitech Forum; 2020 Jan 6–10; Orlando, FL. AIAA Paper No.: 2020-1762.

7. Vasile J, Bryson J, Fresconi F. Aerodynamic design optimization of long-range projectiles using Missile DATCOM. Aberdeen Proving Ground (MD): CCDC Army Research Laboratory (US); 2020 Apr. Report No.: ARL-TR-8936.

8. Bryson J, Vasile J, Gruenwald B, Fresconi F. Control surface design analysis and actuation requirements development for munitions. Proceedings of the AIAA Scitech Forum; 2020 Jan 6–10; Orlando, FL. AIAA Paper No.: 2020-0020.

9. Bryson J, Vasile J, Fresconi F. Control surface design analysis for munitions. Aberdeen Proving Ground (MD): CCDC Army Research Laboratory (US); 2020 Mar. Report No.: ARL-TR-8919.

10. Metacomp Technologies, Inc. MIME user manual. Agoura Hills (CA): Metacomp; 2010.

11. Dey S, Aubry RM, Karamete BK, Mestreau EL. Capstone: a geometry-centric platform to enable physics-based simulation and system design. Computing in Science & Engineering. 2016;18(1):32–39.

12. Sahu J, Fresconi F. Fast generation of aerodynamics data for a canard-controlled body with thrust-vector control. Proceedings of the AIAA Aviation Forum; 2019 June 17–21; Dallas, TX. AIAA Paper No.: 2019-3163.

13. Sahu J, Fresconi F. Flight behaviors of a complex projectile using a coupled CFD-based simulation technique: free motion. Proceedings of the AIAA Aviation Forum; 2015 June 22–25; Dallas, TX. AIAA Paper No.: 2015-2585.

14. Hunt JCR, Wray AA, Moin P. Eddies, streams, and convergence zones in turbulent flows. Stanford (CA): Center for Turbulence Research; 1988. Report No.: CTR-S88. p. 193.

15. Vasile JD, Sahu J. Roll orientation–dependent aerodynamics of a long-range projectile. Aberdeen Proving Ground (MD): CCDC Army Research Laboratory (US); 2020 Aug. Report No.: ARL-TR-9017.

.

List of Symbols, Abbreviations, and Acronyms

3-D	three-dimensional
6DOF	6 degrees of freedom
AMR	adaptive mesh refinement
CFD	computational fluid dynamics
CFL	Courant–Friedrichs–Lewy
DOD	US Department of Defense
DSRC	DOD Supercomputing Resource Center
FAS	fixed aerodynamic surfaces
MAS	movable aerodynamic surfaces
NASA	National Aeronautics and Space Administration
OAL	overall length
RBD	rigid body dynamics
RANS	Reynolds-averaged Navier–Stokes
SEAP	semi-empirical aerodynamic prediction

Nomenclature

α	angle of attack
δ_i	trailing-edge flap deflection for flap i
ϕ	aerodynamic roll angle
M_∞	freestream Mach number
C_A	axial force coefficient
C_N	normal force coefficient
C_S	side force coefficient
C_l	rolling moment coefficient
C_m	pitching-moment coefficient
C_n	yawing moment coefficient
C_{m_q}	pitch-damping coefficient sum (i.e., $C_{m_q} + C_{m_{\dot{\alpha}}}$)
C_{l_p}	roll-damping coefficient
δ_q	trailing-edge flap deflection for pitch deflection
C_X	nonrolled x-axis force coefficient, flight dynamics body frame
C_Y	nonrolled y-axis force coefficient, flight dynamics body frame
C_Z	nonrolled z-axis force coefficient, flight dynamics body frame
Q_S	scaled Q-criterion
$\boldsymbol{\Omega}$	vorticity tensor
$\boldsymbol{S}$	strain tensor

1 (PDF) DEFENSE TECHNICAL
INFORMATION CTR
DTIC OCA

1 (PDF) CCDC ARL
FCDD RLD CL
TECH LIB

1 (PDF) CCDC AC
RDAR-MEM-A
M DUCA

3 (PDF) CCDC AVMC
FCDD AMS MMA
J DOYLE
C ROSEMA
M MCDANIEL

1 (PDF) JHU/APL
A NEDUNGADI

28 (PDF) CCDC ARL
FCDD RLW
J ZABINSKI
FCDD RLW A
F FRESCONI
FCDD RLW L
W OBERLE
P PEREGINO
T SHEPPARD
FCDD RLW LB
N TRIVEDI
E BYRD
FCDD RLW LC
J SADLER
FCDD RLW LD
A WILLIAMS
M NUSCA
A MCBAIN
FCDD RLW LE
J VASILE
J BRYSON
J DESPIRITO
L STROHM
J PAUL
V BHAGWANDIN
L FAIRFAX
B GRUENWALD
I CELMINS
J SAHU
FCDD RLW LF
M ILG
B TOPPER
D EVERSON
T BROWN
FCDD RLW LH
M MINNICINO
R SUMMERS
FCDD RLW ME
S SILTON